Analytical linear theory for the interaction of a planar shock wave with a two- or three-dimensional random isotropic acoustic wave field

C. Huete* and J. G. Wouchuk

Escuela Técnica Superior de Ingenieros Industriales, Instituto de Investigaciones Energéticas (INEI), Universidad de Castilla La Mancha, Campus s/n, E-13071 Ciudad Real, Spain

A. L. Velikovich

Plasma Physics Division, Naval Research Laboratory (NRL), Washington, DC 23075, USA

(Received 19 September 2011; published 15 February 2012)

We present an analytical model that describes the linear interaction of a planar shock wave with an isotropic random sonic field. First, we study the interaction with a single-mode acoustic field. We present the exact evolution for the pressure, velocity, vorticity, and density field generated behind the shock wave, and we also calculate exact and closed analytical expressions for the asymptotic behavior of these modes. Applying superposition, we use the results obtained from the single-mode analysis in order to compute the interaction with 2D/3D isotropic random acoustic fields. We present analytical expressions for the average turbulent kinetic energy generated behind the shock, as well as the averaged vorticity and the density perturbations as a function of the shock strength M_1 and the gas compressibility γ. We also study the acoustic energy flux emitted by the shock front. Exact asymptotic analytical scaling laws are given for all the 3D averages downstream. A detailed comparison with previous works is shown.

DOI: 10.1103/PhysRevE.85.026312 PACS number(s): 47.40.Nm, 47.27.Sd, 47.27.Gs

I. INTRODUCTION

The propagation of shock waves in inhomogeneous/turbulent flows is a fundamental problem in different fields, ranging from shock tube research [1–3], astrophysics [4], aerodynamics [5–12], inertial confinement fusion (ICF), and high energy density physics (HEDP), where the shock waves traveling into an inhomogeneous medium generate additional vorticity, density, and pressure downstream fluctuations that may affect shock performance [13–16]. The subject has been under study for more than 50 years, beginning with the pioneering works of Ribner on the interaction of a shock wave with vortical flows [5,7] and of Moore [6] on the interaction of a shock front with acoustic waves. With the advent of supercomputers, the theoretical investigation benefited from the development of hydrodynamic simulation that resulted in large eddy simulations (LES) as in Ref. [13] or direct numerical simulations (DNS) as in Ref. [11]. Good agreement with the existing linear analysis of the same problem has been obtained. Nevertheless, a complete and general study of the downstream quantities as functions of the fluid compressibility and shock strength could not be presented in those works. Quite recently, linear theoretical models for the interaction of a shock wave with an isentropic vorticity field [17] and with an isotropic density field [18–20] have been reported, where such an extensive study of the downstream quantities (turbulent kinetic energy, acoustic flux, vorticity, density) was done. Exact analytical expressions for arbitrary values of the shock Mach number and fluid compressibility were obtained for the quantities of interest behind the shock in terms of elementary functions, completing the work started more than 50 years ago. Regarding the interaction of a shock wave with an isotropic field of acoustic waves, there is only the study reported in Ref. [10], which showed a comparison between their numerical results and the linear theory predictions based on the theory developed by Moore [6]. The present work is a natural continuation of the works shown in Refs. [17,19], and the goal is to describe the generation of vorticity, pressure, and density perturbations downstream due to the influence of an isotropic field of acoustic waves in front of the shock [see Fig. 1(a)], and their dependence upon the fluid compressibility and the shock strength [21]. This work is a necessary step, not only to complete the picture of the linear shock interaction with the three fundamental hydrodynamic perturbation modes, but also to gain a basic understanding in order to deal with the reshock of arbitrary turbulent flows. Generally speaking, a first shock launched against any of the three different problems mentioned above will generate the three perturbation modes behind it. Consequently, any second shock launched after the first one will interact with all three perturbation modes simultaneously. Each mode interacts in its own way with the shock front. Therefore, it is very convenient to have the three problems studied separately before the more complex problem of reshocking a complete turbulent field (with entropic, vortical, and acoustic perturbations in it) is considered.

In Sec. II, we consider the interaction of the shock wave with a single two-dimensional (2D) mode upstream in order to identify the basic mechanisms of downstream perturbation generation (pressure, vorticity, velocity, acoustic flux), assuming an ideal-gas equation of state. The Richtmyer-Meshkov (RM) unstable growth at the weak discontinuity is also studied in detail. A particular case, in which the upstream acoustic waves only travel along the x axis, is studied by means of the characteristic method in Appendix A. Later on, in Sec. III, mode averaging is performed as usual in order to calculate the statistical averages downstream, to take into account the interaction of a planar shock front with a full spectrum of

*cesar.huete@uclm.es

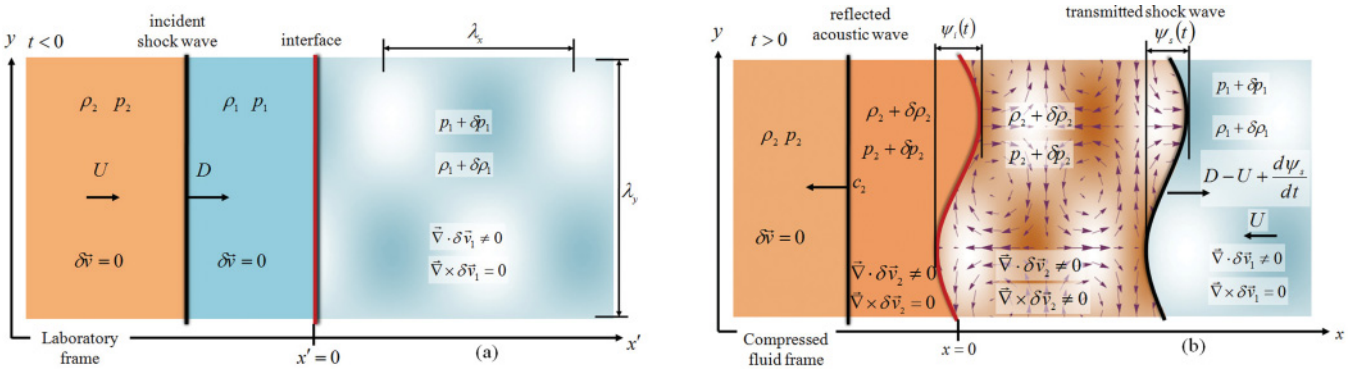

FIG. 1. (Color online) (a) The incident planar shock travels with velocity $D\hat{x}$ in the laboratory reference frame for $t < 0$. (b) The transmitted corrugated shock moves into the disturbed fluid at the compressed fluid frame for $t > 0$ with velocity $(D - U)\hat{x}$. Density, vorticity, and acoustic fluctuations are generated behind it. A stable sound wave is reflected to the left and it travels with velocity c_2 in this frame.

randomly oriented acoustic waves. Mode averaging is done in both two and three dimensions. Exact asymptotic expressions are obtained in the important physical limits of weak shocks, strong shocks, and highly compressible fluids, thus completing the study initiated in Ref. [10]. Turbulent kinetic energy, acoustic flux, vorticity, density, and the level of anisotropy of the velocity perturbations are systematically studied as functions of the fluid compressibility and the shock Mach number. All these quantities are analyzed in the asymptotic limits, and exact expressions are given in terms of elementary functions of the Mach number and adiabatic index γ (the ratio of specific heats) in Appendix B. Finally, a summary is presented in Sec. IV.

II. INTERACTION OF A PLANAR SHOCK WITH A SINGLE-MODE 2D ACOUSTIC FIELD

A. Wave equation and boundary conditions

In this section, we consider the interaction of an isolated shock wave with a single-mode 2D acoustic perturbed field. We choose the time origin such that the shock is incident at $t = 0$ at the surface $x' = 0$ in the laboratory frame. The fluid is an ideal gas with adiabatic exponent γ. The shock comes from the left ($x' = -\infty$) and travels with velocity $D\hat{x}'$, as measured in the laboratory frame. In the uniform half-space $x' < 0$, the density and pressure ahead of the shock are ρ_1 and p_1 respectively, and ρ_2 and p_2 are the values behind it. The velocity of the compressed fluid is $U\hat{x}'$, also measured in the laboratory. The upstream sound speed is c_1 and its downstream value is c_2. The shock Mach number with respect to the upstream gas is $M_1 = D/c_1 \geqslant 1$ and the shock Mach number with respect to the compressed fluid is $M_2 = (D - U)/c_2 \leqslant 1$. We denote the upstream values with the subscript 1 and the downstream values with the subscript 2 [see Fig. 1(a)]. Before the shock arrives at the interface $x' = 0$, the quantities at both sides of the shock front are related by

$$R = \frac{\rho_2}{\rho_1} = \frac{D}{D-U} = \frac{(\gamma+1)M_1^2}{(\gamma-1)M_1^2+2}, \tag{1}$$

$$M_2 = \frac{D-U}{c_2} = \sqrt{\frac{(\gamma-1)M_1^2+2}{2\gamma M_1^2-\gamma+1}}, \tag{2}$$

$$\frac{p_2}{p_1} = \frac{2\gamma M_1^2-\gamma+1}{\gamma+1}, \tag{3}$$

$$\frac{c_2}{c_1} = \frac{\sqrt{(2\gamma M_1^2-\gamma+1)[(\gamma-1)M_1^2+2]}}{(\gamma+1)M_1}. \tag{4}$$

In the right half-space, the perturbed acoustic field is described by

$$\begin{aligned}
\delta p_1(x',y,t) &= \rho_1 c_1^2 \sigma_k \cos(k_x x' - \omega_1 t)\cos(k_y y),\\
\delta \rho_1(x',y,t) &= \rho_1 \sigma_k \cos(k_x x' - \omega_1 t)\cos(k_y y),\\
\delta v_{x1}(x',y,t) &= c_1 \cos\theta \sigma_k \cos(k_x x' - \omega_1 t)\cos(k_y y),\\
\delta v_{y1}(x',y,t) &= -c_1 \sin\theta \sigma_k \sin(k_x x' - \omega_1 t)\sin(k_y y),
\end{aligned} \tag{5}$$

where the wave-number vector is defined as

$$\vec{k} = (k_x, k_y) = |\vec{k}|(\cos\theta, \sin\theta) \tag{6}$$

and the frequency of the particle oscillations ω_1 is

$$\omega_1 = c_1\sqrt{k_x^2 + k_y^2}. \tag{7}$$

To remain within the limits of validity of the linear theory, we assume $\sigma_k \ll 1$, and that it is only a function of $k = \sqrt{k_x^2 + k_y^2}$. Once the shock is in the half-space $x' \geqslant 0$, the density profile in front of it will induce density, pressure, and velocity fluctuations downstream, and its shape will be distorted [see Fig. 1(b)]. From now on, the fluid equations will be solved in the system of reference comoving with the compressed medium where the longitudinal coordinate is now indicated by "x."

We define the downstream dimensionless perturbations, factoring out the small parameter σ_k:

$$\begin{aligned}
\delta p_2 &= \rho_2 c_2^2 \sigma_k \tilde{p}(x,t)\cos(k_y y),\\
\delta \rho_2 &= \rho_2 \sigma_k \tilde{\rho}(x,t)\cos(k_y y),\\
\delta v_{2x} &= c_2 \sigma_k \tilde{v}_x(x,t)\cos(k_y y),\\
\delta v_{2y} &= c_2 \sigma_k \tilde{v}_y(x,t)\sin(k_y y),\\
\delta \omega_{2z} &= k_y c_2 \sigma_k \tilde{\omega}_z \sin(k_y y).
\end{aligned} \tag{8}$$

In Eq. (8), t is the time and x is the longitudinal coordinate as measured in the compressed fluid frame. The quantities $\tilde{v}_x$ and $\tilde{v}_y$ correspond to the longitudinal and transverse velocities,

respectively, and $\tilde{\rho}$ and $\tilde{p}$ represent the dimensionless density and pressure perturbations. The function $\tilde{\omega}_z$ indicates the dimensionless vorticity generated behind the shock. We also define the dimensionless time $\tau = k_y c_2 t$. The linearized equations of motion in the compressed fluid frame, in dimensionless form, are

$$\begin{aligned} \frac{\partial \tilde{\rho}}{\partial \tau} &= -\frac{\partial \tilde{v}_x}{\partial (k_y\, x)} - \tilde{v}_y, \\ \frac{\partial \tilde{v}_x}{\partial \tau} &= -\frac{\partial \tilde{p}}{\partial (k_y\, x)}, \\ \frac{\partial \tilde{v}_y}{\partial \tau} &= \tilde{p}, \end{aligned} \tag{9}$$

representing, the mass, x-momentum, and y-momentum conservation equations, respectively. Furthermore, the conservation of entropy holds if we assume adiabatic flow behind the shock, which leads us to

$$\frac{\partial \tilde{p}}{\partial \tau} = \frac{\partial \tilde{\rho}}{\partial \tau}. \tag{10}$$

The dynamics of the perturbed quantities in the whole compressed fluid is governed by the wave equation. Combining the above conservation equations (9) and using Eq. (10), we get the wave equation:

$$\frac{\partial^2 \tilde{p}}{\partial \tau^2} = \frac{\partial^2 \tilde{p}}{\partial (k_y x)^2} - \tilde{p}. \tag{11}$$

At $t = 0^+$, a shock is transmitted to the right into the perturbed half-space and a neutrally stable sound wave is reflected back inside the region $x < 0$, as shown in Fig. 1(b). As the shock wave travels in a nonuniform fluid, the shock shape will be corrugated. We therefore define the shock ripple amplitude as $\psi_s(y,t)$, which measures its deviation from planarity. The shock ripple oscillates in time, generating pressure fluctuations that propagate with the local sound speed into the compressed fluid. The sound waves generated by the shock oscillation can be stable or evanescent, depending on the ratio k_x/k_y, the shock Mach number M_1, and the gas compressibility γ [15,17,19]. As a downstream boundary condition, we assume that no sound wave hits the shock surface from behind, that is, the shock travels isolated. At the surface $x = 0$, pressure and normal velocity are continuous. However, the distorted front generates vorticity and entropy perturbations and the neutral sound wave to the left does not. Hence, the x derivatives of $\tilde{v}_y$ and $\tilde{\rho}$ are discontinuous at $x = 0$. It is not difficult to get the following relationships just to the right of the left-traveling sound wave [17,19]:

$$\begin{aligned} \tilde{v}_x + \tilde{p} &= 0, \\ \tilde{v}_y &= 0. \end{aligned} \tag{12}$$

The boundary conditions at the shock are obtained after linearizing the Rankine-Hugoniot (RH) conditions and using the continuity of the tangential velocity. We write them here for the particular case of preshock acoustic modulation:

$$\frac{d\xi_s}{d\tau} = \frac{\gamma+1}{4M_2}\tilde{p}_2 - \frac{M_2 R}{2}\tilde{\rho}_1 + \frac{M_2 R}{M_1}\tilde{v}_{x1} + \frac{R M_2(\gamma-1)}{4M_1^2}\tilde{p}_1, \tag{13}$$

$$\tilde{v}_{x2} = \frac{M_1^2+1}{2M_1^2 M_2}\tilde{p}_2 - \frac{M_2(R-1)}{2}\tilde{\rho}_1 + \frac{M_2 R}{M_1}\tilde{v}_{x1} - \frac{R M_2^2+1}{2M_2 M_1^2}\tilde{p}_1, \tag{14}$$

$$\tilde{v}_{y2} = M_2(R-1)\xi_s + \frac{M_2 R}{M_1}\tilde{v}_{y1}, \tag{15}$$

$$\tilde{\rho}_2 = \frac{1}{M_1^2 M_2^2}\tilde{p}_2 + \tilde{\rho}_1 - \frac{1}{M_1^2 M_2^2}\tilde{p}_1, \tag{16}$$

where Eq. (13) represents the mass conservation equation, Eqs. (14) and (15) correspond to the longitudinal and transverse momentum conservation, respectively, and Eq. (16) is the energy equation. Here, ξ_s is the dimensionless shock ripple amplitude, defined by $\xi_s \sigma_k = k_y \psi_s$.

1. *Initial and boundary conditions*

To get the perturbed quantities in the compressed fluid, we solve the wave equation (11) together with the adequate boundary conditions. To this end, we need to specify them at the weak discontinuity ($x = 0$) and at the shock front [$x = x_s(t) = (D-U)t$]. We need the initial value of the pressure perturbation behind the shock to solve the complete temporal dynamics of the shock front perturbation. Using Eqs. (12)–(16), it is easy to see that

$$\tilde{p}_{s0} = \frac{M_2^2 R + 1 + M_2^2 M_1^2 (R-1) - 2M_2^2 M_1 R\cos\theta}{2M_1^2 M_2 + M_1^2 + 1}\sigma_k, \tag{17}$$

where $\tilde{p}_{s0}$ is the initial shock pressure perturbation at $t = 0^+$. Furthermore, it is clear that the initial shock ripple amplitude is $\xi_{s0} \equiv 0$, as the shock front is planar in shape when it arrives at $x = 0$. As we have seen before, the distorted shock front is a moving boundary and it is convenient to solve the fluid equations by means of the coordinate transformation suggested in Ref. [22] and used in Refs. [17,19,23,24]:

$$\begin{aligned} k_y x &= r\sinh\chi, \\ \tau &= r\cosh\chi. \end{aligned} \tag{18}$$

It is straightforward to see that $\chi = \text{const}$ represents a planar front defined by $x = c_2 t\tanh\chi$. The shock front coordinate is therefore given by $\tanh\chi_s = M_2$, and from Eq. (18) we get

$$\tau = r_s\cosh\chi_s = \frac{r_s}{\sqrt{1-M_2^2}}. \tag{19}$$

The wave equation (11) is now rewritten as

$$r\frac{\partial^2 \tilde{p}}{\partial r^2} + \frac{\partial \tilde{p}}{\partial r} + r\tilde{p} = \frac{\partial \tilde{h}}{\partial \chi}, \tag{20}$$

where $\tilde{h}$ is an auxiliary function defined by

$$\tilde{h} = \frac{1}{r}\frac{\partial \tilde{p}}{\partial \chi}. \tag{21}$$

The boundary conditions at the shock front Eqs. (13)–(16) can be recast as

$$\frac{1}{r_s}\left(\frac{\partial\tilde{p}}{\partial\chi}\right)_{\chi_s} = -\frac{M_1^2+1}{2M_1^2M_2}\frac{d\tilde{p}_s}{dr_s} - \frac{M_2^2(R-1)}{\sqrt{1-M_2^2}}\xi_s - \sigma_k\frac{A_\sigma}{\sqrt{1-M_2^2}}\sin(\zeta_{\rm ac}r_s), \tag{22}$$

$$\frac{d\xi_s}{dr_s} = \frac{\gamma+1}{4M_2\sqrt{1-M_2^2}}\tilde{p}_s + \sigma_k\frac{B_\sigma}{\sqrt{1-M_2^2}}\cos(\zeta_{\rm ac}r_s), \tag{23}$$

where the coefficients A_σ and B_σ are

$$A_\sigma = \left[\frac{M_2^2R + M_1^2M_2^2(R-1)+1}{2M_2M_1^2} - \frac{M_2R}{M_1}\cos\theta\right] \times \left(\cos\theta - \frac{1}{M_1}\right)\frac{RM_2}{\sin\theta} - \frac{M_2^2R}{M_1}\sin\theta, \tag{24}$$

$$B_\sigma = \left(\frac{\gamma-2M_1^2-1}{4M_1^2}\right)M_2R + \frac{M_2R}{M_1}\cos\theta, \tag{25}$$

and where $\zeta_{\rm ac}$ is a dimensionless frequency that characterizes the periodicity of the preshock density inhomogeneity. Its value is given by

$$\zeta_{\rm ac} = \left(\cos\theta - \frac{1}{M_1}\right)\frac{RM_2}{\sqrt{1-M_2^2}}\frac{1}{\sin\theta}, \tag{26}$$

where $(0<\theta<\pi)$ and $(-\infty<\zeta_{\rm ac}<\infty)$. For steady perturbations in front of the shock such as those studied in Refs. [15,17–19], modes with inclinations θ and $\pi-\theta$ would induce the same oscillation frequency at the shock front. However, for the case studied here, a sound wave moving upstream with $0<\theta<\pi/2$ has a lower relative velocity to the shock wave than the sound wave with its wave-number vector oriented with $\pi-\theta$. Thus, the two acoustic fronts would make the shock oscillate with different frequencies, and the corresponding dimensionless frequencies $\zeta_{\rm ac}$ will be different for the two orientations. If we consider a very strong shock, the term $1/M_1$ can be dropped in the above formula and we see that $\zeta_{\rm ac}$ is equivalent to the dimensionless frequency of the preshock vorticity [17] and preshock density [19] problems. Furthermore, in the very strong shock limit, also the linearized RH equations become equal for the preshock density problem and the preshock acoustic case considered here. Therefore, we expect to get the same scaling laws for the downstream quantities at very large Mach numbers, either for entropic perturbations or acoustic waves upstream. This is natural, because for very strong shocks, it is $D \gg c_1$ and the shock front "sees" essentially frozen perturbations in both cases. From Eq. (26), we see that the incidence angle θ can also be thought of as a function of $\zeta_{\rm ac}$. In fact, it is convenient for future calculations to express θ as

$$\cos\theta = \frac{R^2M_2^2}{M_1\left[R^2M_2^2+\zeta_{\rm ac}^2(1-M_2^2)\right]} \times \left(1+\zeta_{\rm ac}\frac{M_1\sqrt{1-M_2^2}}{RM_2}\sqrt{\frac{1-M_2^2}{R^2M_2^2}\zeta_{\rm ac}^2+\frac{M_1-1}{M_1}}\right) \tag{27}$$

or, equivalently,

$$\sin\theta = -\frac{RM_2\sqrt{1-M_2^2}}{M_1\left[R^2M_2^2+\zeta_{\rm ac}^2(1-M_2^2)\right]} \times \left(\zeta_{\rm ac} - \frac{RM_1M_2}{\sqrt{1-M_2^2}}\sqrt{\frac{1-M_2^2}{R^2M_2^2}\zeta_{\rm ac}^2+\frac{M_1-1}{M_1}}\right). \tag{28}$$

2. *Laplace transform*

In order to solve the wave equation (20) and the linearized RH [Eqs. (22) and (23)], we use the Laplace transform over the variable r. We define the Laplace transform of any quantity ϕ:

$$\Phi(\chi,s) = \int_0^\infty \phi(\chi,r)\exp(-sr)dr. \tag{29}$$

We use the variable q defined by $s=\sinh q$, and then the wave equation (20) together with Eq. (21) can be rewritten as

$$\begin{aligned}\frac{\partial}{\partial q}(\cosh q\ \tilde{P}) + \frac{\partial\tilde{H}}{\partial\chi} &= 0,\\ \frac{\partial}{\partial\chi}(\cosh q\ \tilde{P}) + \frac{\partial\tilde{H}}{\partial q} &= 0.\end{aligned} \tag{30}$$

After some algebra, the following decomposition for the pressure ($\tilde{P}$) and pressure gradient ($\tilde{H}$) is obtained [22,24]:

$$\begin{aligned}\tilde{P}(\chi,q) &= \frac{F_1(q-\chi)+F_2(q+\chi)}{\cosh q},\\ \tilde{H}(\chi,q) &= F_1(q-\chi)-F_2(q+\chi),\end{aligned} \tag{31}$$

where the functions F_1 and F_2 must be determined with the help of the boundary and initial conditions. As was demonstrated in previous works [24], F_1 represents the sound waves emitted by the shock front and F_2 represents the sound waves that arrive at the shock front from behind [22,25]. In our case, where the shock is isolated, F_2 is a constant, and its value is determined with the aid of the initial conditions Eq. (17). At the shock front, the following equation holds:

$$\tilde{H}_s(q) = \cosh q\,\tilde{P}_s q - 2F_2. \tag{32}$$

We also transform Eqs. (22) and (23) by using the Laplace transform:

$$\tilde{H}_s(s) = -\frac{M_1^2+1}{2M_1^2M_2}[s\tilde{P}_s(s)-\tilde{p}_{s0}] - \frac{M_2^2(R-1)}{\sqrt{1-M_2^2}}\bar{\xi}_s - \sigma_k\frac{A_\sigma}{\sqrt{1-M_2^2}}\frac{\zeta_{\rm ac}}{s^2+\zeta_{\rm ac}^2}, \tag{33}$$

$$s\bar{\xi}_s(s)-\xi_{s0} = \frac{\gamma+1}{4M_2\sqrt{1-M_2^2}}\tilde{P}_s(s) + \sigma_k\frac{B_\sigma}{\sqrt{1-M_2^2}}\frac{s}{s^2+\zeta_{\rm ac}^2}, \tag{34}$$

where $\bar{\xi}_s = \int_0^\infty \xi_s(r)\exp(-sr)dr$. In our case, $\xi_{s0} = 0$, because the shock shape is planar when it reaches the perturbed region ($x' \geqslant 0$). Using Eq. (32), it can be seen that $2F_2 = \tilde{p}_{s0}$. After some additional algebra, we get an exact closed-form expression for the Laplace transform of the shock front pressure fluctuations $\tilde{P}_s$, given by

$$\tilde{P}_s(s) = \frac{\left(M_1^2 + 1 + 2M_1^2M_2\right)\tilde{p}_{s0}\, s}{2M_1^2M_2 s\sqrt{s^2+1} + \left(M_1^2+1\right)s^2 + M_1^2} + \frac{2M_1^2M_2\,\alpha_\sigma\, s}{\left[2M_1^2M_2 s\sqrt{s^2+1} + \left(M_1^2+1\right)s^2 + M_1^2\right]\left(s^2+\zeta_{ac}^2\right)}. \tag{35}$$

The coefficient α_σ is given by

$$\alpha_\sigma = -\sigma_k \frac{\sqrt{1-M_2^2}A_\sigma\zeta_{ac} + M_2^2(R-1)B_\sigma}{1-M_2^2}, \tag{36}$$

where A_σ and B_σ are defined in Eqs. (24) and (25).

3. *Inverse Laplace transform*

The complete evolution of the shock pressure perturbations as a function of the dimensionless time τ is obtained by means of the inverse Laplace transform of Eq. (35), after an integration in the complex plane. We formally write

$$\tilde{p}_s(r_s) = \frac{1}{2\pi i}\int_{b-i\infty}^{b+i\infty} \tilde{P}_s(s)\exp(sr_s)ds, \tag{37}$$

where b is a real number to the right of the singularities of $\tilde{P}_s(s)$, and i is the imaginary unit ($i^2 = -1$). To get an algebraic expression from (37), we close the integration contour to the left and use the residue theorem, taking care of the singularities enclosed by the integration path. For a shock moving into an ideal gas, the only singularities of $\tilde{P}_s(s)$, as can be seen from Eq. (35), are the branch points at $s = \pm i$ and the poles at $s = \pm i\zeta_{ac}$ [17,19]. The branch point singularities represent the generation of evanescent sound wave perturbations, which decay asymptotically in time like $t^{-3/2}$, in much the same way as Bessel functions. On the other hand, the imaginary poles give rise to asymptotic constant amplitude oscillations. These permanent oscillations of the shock ripple are due to the perturbations in velocity distributed periodically upstream. In addition, the denominator $2M_1^2M_2s\sqrt{s^2+1} + (M_1^2+1)s^2 + M_1^2$ never contributes with additional singularities that could result in permanent oscillations for an ideal-gas equation of state [25]. After some algebra, we get

$$\tilde{p}_s(r_s) = -\frac{2\tilde{p}_{s0}}{\pi}\int_0^1 f_p(z)\cos(zr_s)dz + \frac{2\alpha_\sigma}{\pi}\int_0^1 f_p(z) \times \left[\frac{\cos(zr_s) - \cos(\zeta_{ac}r_s)}{\zeta_{ac}^2 - z^2}\right]dz, \tag{38}$$

where the auxiliary function f_p is given by

$$f_p(z) = \frac{4M_1^4M_2^2z^2\sqrt{1-z^2}}{4M_1^2M_2^2z^2(1-z^2) + \left[\left(M_1^2+1\right)z^2 - M_1^2\right]^2}. \tag{39}$$

The asymptotic behavior of $\tilde{p}_s$ can be calculated by studying the residues of Eq. (35) at the imaginary poles $s = \pm i\zeta_{ac}$. The modes that have $|\zeta_{ac}| < 1$ are called long-wavelength modes and the modes with $|\zeta_{ac}| > 1$ are called short-wavelength modes, as done in previous works [17,19]. The reason will become apparent later on when studying the sound emission downstream by the corrugated shock front. With the help of the exact Laplace transform of the shock pressure perturbations Eq. (35), it is not difficult to obtain the time asymptotic for both branches:

$$\tilde{p}_s(\tau \gg 1) \cong \begin{cases} e_{l1}\cos(\zeta_{ac}r_s) + e_{l2}\sin(\zeta_{ac}r_s), & |\zeta_{ac}| \leqslant 1, \\ e_s\cos(\zeta_{ac}r_s), & |\zeta_{ac}| \geqslant 1, \end{cases} \tag{40}$$

where $r_s = \tau\sqrt{1-M_2^2}$, and the coefficients e_{l1}, e_{l2}, and e_s are

$$e_{l1} = \frac{2M_1^2M_2\left[M_1^2 - \left(M_1^2+1\right)\zeta_{ac}^2\right]\alpha_\sigma}{4M_1^4M_2^2\zeta_{ac}^2\left(1-\zeta_{ac}^2\right) + \left[M_1^2 - \left(M_1^2+1\right)\zeta_{ac}^2\right]^2},$$
$$e_{l2} = \frac{4M_1^4M_2^2\zeta_{ac}\sqrt{1-\zeta_{ac}^2}\,\alpha_\sigma}{4M_1^4M_2^2\zeta_{ac}^2\left(1-\zeta_{ac}^2\right) + \left[M_1^2 - \left(M_1^2+1\right)\zeta_{ac}^2\right]^2}, \tag{41}$$
$$e_s = -\frac{2M_1^2M_2\,\alpha_\sigma}{2M_1^2M_2\zeta_{ac}\sqrt{\zeta_{ac}^2-1} + \left(M_1^2+1\right)\zeta_{ac}^2 - M_1^2}.$$

The coefficients e_{l1}, e_{l2}, and e_s are formally equivalent to those shown in Eq. (47) in Ref. [17] and Eq. (26) in Ref. [19]. The only difference lies in the different values of α_σ here Eq. (36) and α_v and α_e in Refs. [17,19], respectively. In Fig. 2(a), we plot the shock pressure evolution for the long-wavelength regime ($|\zeta_{ac}| < 1$) for an incident shock with $M_1 = 2$ that travels through air ($\gamma = 7/5$), and the incoming sonic front

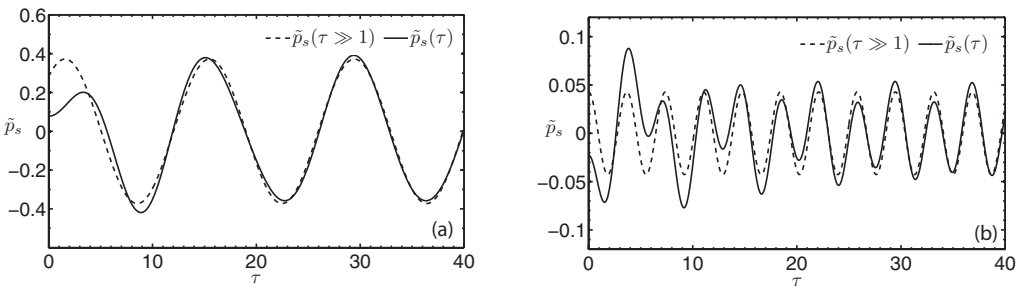

FIG. 2. Asymptotic and exact shock pressure ($\tilde{p}_s$) for an ideal gas with adiabatic index $\gamma = 7/5$ and shock strength $M_1 = 2.0$, and an incident angle of $\theta = \pi/4$ corresponding to $\zeta_{ac} = 0.552\,285$ (a) and $\theta = \pi/8$ corresponding to $\zeta_{ac} = 2.088\,61$ (b).

upstream is oriented with $\theta = \pi/4$, whereas in Fig. 2(b) we are in the short-wavelength regime ($|\zeta_{\rm ac}| > 1$), with an incident angle $\theta = \pi/8$. We can also calculate the analytical expression for the shock ripple evolution. If we integrate Eq. (13) in time, we obtain

$$\xi_s(r_s) = \frac{(\gamma+1)\tilde{p}_{s0}}{\pi M_2\sqrt{1-M_2^2}}\int_0^1 \frac{f_p(z)}{z}\sin(zr_s)dz + \frac{\beta_\sigma}{\zeta_{\rm ac}\sqrt{1-M_2^2}}\sin(\zeta_{\rm ac}r_s) + \frac{(\gamma+1)\alpha_\sigma}{\pi M_2\sqrt{1-M_2^2}} \times \int_0^1 \frac{f_p(z)}{\zeta_{\rm ac}^2 - z^2}\left[\frac{\sin(zr_s)}{z} - \frac{\sin(\zeta_{\rm ac}r_s)}{\zeta_{\rm ac}}\right]dz. \quad (42)$$

The asymptotic expression for the shock front ripple can also be easily obtained substituting (35) into (13) and integrating,

$$\xi_s(r_s) \cong \begin{cases} j_{I1}\sin(\zeta_{\rm ac}r_s) + j_{I2}\cos(\zeta_{\rm ac}r_s), & |\zeta_{\rm ac}| \leqslant 1, \\ j_s\sin(\zeta_{\rm ac}r_s), & |\zeta_{\rm ac}| \geqslant 1. \end{cases} \quad (43)$$

The coefficients are

$$j_{I1} = \frac{\beta_\sigma + e_{I1}}{\zeta_{\rm ac}\sqrt{1-M_2^2}}, \quad j_{I2} = -\frac{e_{I2}}{\zeta_{\rm ac}\sqrt{1-M_2^2}}, \quad j_s = \frac{\beta_\sigma + e_s}{\zeta_{\rm ac}\sqrt{1-M_2^2}}. \quad (44)$$

B. Sound waves emitted by the shock front downstream

1. Pressure perturbations of the running acoustic waves emitted downstream when $|\zeta_{ac}| > 1/\sqrt{1-M_2^2}$

In the preceding subsection, we have shown how the shock oscillations generate pressure perturbations at the shock front. In the domain of the variable r_s, the shock oscillates with dimensionless frequency $\zeta_{\rm ac}$. If $\zeta_{\rm ac} < 1$, the pressure perturbations generated by the shock wave are evanescent and decay in time like $t^{-3/2}$ at any position behind the shock. Nevertheless, in the short-wavelength regime ($\zeta_{\rm ac} > 1$), the sound waves can escape from the shock front filling the space behind it in the form of stable traveling fronts. To understand the behavior of the pressure field downstream, we make a more detailed study of the information provided by the Laplace transform $\tilde{P}(\chi,q)$. In the following discussion, we concentrate on the situation with $|\zeta_{\rm ac}| > 1$. In fact, we write the Laplace function $\tilde{P}$ at any given value of the coordinate χ:

$$\tilde{P}(\chi,q) = \frac{\cosh(q+\chi_s-\chi)}{\cosh q}\tilde{P}_s(q+\chi_s-\chi), \quad (45)$$

where it is not difficult to realize [see Eq. (35)] that the right-hand side has a denominator of the form

$$\sinh^2(q+\chi_s-\chi) + \zeta_{\rm ac}^2 = [\sinh(q+\chi_s-\chi) + i\zeta_{\rm ac}][\sinh(q+\chi_s-\chi) - i\zeta_{\rm ac}]. \quad (46)$$

After some additional algebra, we see that this term would contribute with imaginary poles at certain imaginary complex values for the Laplace variable s, which we call $s = \pm i\zeta_\chi$ (hence contributing with constant amplitude oscillations) if and only if the following relationship holds:

$$|\zeta_{\rm ac}| \geqslant \cosh(\chi_s - \chi). \quad (47)$$

If condition Eq. (47) is fulfilled, the mathematical surface defined by $x/t = c_2\tanh\chi$ exhibits stable pressure oscillations. The frequency of those oscillations in the domain of the separable coordinates r,χ, which we named ζ_χ, is obtained by solving the following equation: $\sinh(q+\chi_s-\chi) = i\zeta_{\rm ac}$ (we remind the reader that $\sinh q = \zeta_\chi$). We define $\epsilon_{\rm ac}$ by $|\zeta_{\rm ac}| = \cosh\epsilon_{\rm ac}$ and obtain

$$\zeta_\chi = \cosh(\epsilon_{\rm ac} - \chi_s + \chi) = \cosh(\epsilon_{\rm ac} - \chi_s)\cosh\chi + \sinh(\epsilon_{\rm ac} - \chi_s)\sinh\chi. \quad (48)$$

Therefore, the asymptotic pressure perturbations at any value of χ are given by

$$\tilde{p}(\chi,r) \cong e_s\cos(\zeta_\chi r) = e_s\cos[\cosh(\epsilon_{\rm ac}-\chi_s)\tau - \sinh(\chi_s - \epsilon_{\rm ac})k_y x]. \quad (49)$$

Here, e_s is the asymptotic amplitude of the pressure perturbations at the shock front defined in Eq. (41). Looking inside the argument of the last equation, we realize that the function given in Eq. (49) represents propagating planar fronts in the (x,τ) plane. If $0 < \epsilon_{\rm ac} < \chi_s$ (equivalently $1 < |\zeta_{\rm ac}| < \cosh\chi_s = 1/\sqrt{1-M_2^2}$), the waves are emitted to the right, which then follow the shock front with a streamwise speed given by $c_2M_2\tanh\chi < c_2M_2$. This last result is consistent with the fact that no sound waves impinge on the shock from behind. On the other hand, if $|\zeta_{\rm ac}| > \cosh\chi_s$ (equivalently $\epsilon_{\rm ac} > \chi_s$), the sound waves are emitted to the left. In the absence of a reflecting surface at $x = 0$, those waves escape toward $x = -\infty$. The above Eq. (49) can be rewritten as

$$\tilde{p}(x,\tau) = e_s\cos\left(\zeta_1\tau - k_x^{\rm ac}x\right), \quad (50)$$

where the frequency of oscillation of the compressed fluid particles downstream (when $|\zeta_{\rm ac}| > 1$) can be seen to be equal to

$$\zeta_1 = \frac{\zeta_{\rm ac} - M_2\sqrt{\zeta_{\rm ac}^2 - 1}}{\sqrt{1-M_2^2}}, \quad (51)$$

and the longitudinal downstream wave acoustic wave number $k_x^{\rm ac}$ is

$$\frac{k_x^{\rm ac}}{k_y} = \frac{M_2\zeta_{\rm ac} - \sqrt{\zeta_{\rm ac}^2 - 1}}{\sqrt{1-M_2^2}}. \quad (52)$$

Note the close formal analogy with Eqs. (54) and (55) of Ref. [17] and Eqs. (29) and (30) of Ref. [19].

There are three characteristic values for $|\zeta_{\rm ac}|$. If $|\zeta_{\rm ac}| = 0$, then the upstream longitudinal wave number $k_x = 0$, which means that the perturbations ahead of the shock consist in sonic waves running parallel to the shock front. This particular case has been studied in detail in Ref. [15]. The opposite case is when $k_y = 0$, which corresponds to $|\zeta_{\rm ac}| = \infty$. This situation arises for upstream sonic waves traveling along the longitudinal axis, either impinging on the shock wave or trying to escape from it. For this case, the downstream perturbation field is 1D as there is not transverse flow, and the dynamics of these perturbations can be also obtained by using the

Riemann invariants as discussed in Ref. [26] for linear acoustic perturbations. It is easy to see that this approach gives the same results as Eqs. (41) and (51) for the short-wavelength branch for the case of $|\zeta_{ac}| = \infty$ (see Appendix A).

2. *Critical angles*

It is clear that each value of ζ_{ac} corresponds to a particular value of the the angle θ that the wave-number vector $\vec{k}$ of the incoming sound wave upstream forms with the x axis. The condition $|\zeta_{ac}| > 1$ is equivalent to saying that θ belongs to any of the two intervals $0 < \theta < \theta_1$ or $\theta_2 < \theta < \pi$. The values of θ_1 and θ_2 can be obtained from Eqs. (27) and (28), by making $\zeta_{ac} = \pm 1$, and are given by

$$\begin{aligned}\cos\theta_1 &= \frac{(\gamma+1)M_1^3}{2\gamma M_1^4 - \gamma M_1^2 + 3M_1^2 - 2} \\ &\quad + \frac{\left(M_1^2-1\right)\left(\gamma M_1^2 - M_1^2 + 2\right)}{2\gamma M_1^4 - \gamma M_1^2 + 3M_1^2 - 2}\sqrt{\frac{2\left(\gamma M_1^2+1\right)}{\gamma M_1^2 - M_1^2 + 2}}, \\ \cos\theta_2 &= \frac{(\gamma+1)M_1^3}{2\gamma M_1^4 - \gamma M_1^2 + 3M_1^2 - 2} \\ &\quad - \frac{\left(M_1^2-1\right)\left(\gamma M_1^2 - M_1^2 + 2\right)}{2\gamma M_1^4 - \gamma M_1^2 + 3M_1^2 - 2}\sqrt{\frac{2\left(\gamma M_1^2+1\right)}{\gamma M_1^2 - M_1^2 + 2}}.\end{aligned} \tag{53}$$

Both values agree with the expression given in Eq. (3) of Ref. [10]. The angles θ_1 and θ_2 are called critical angles. Upstream modes with angles between θ_1 and θ_2 do not generate traveling waves downstream, as their perturbations run parallel to the shock surface and decay in the longitudinal direction [15,17,19]. However, for $0 < \theta < \theta_1$ or $\theta_2 < \theta < \pi$, the shock oscillates and radiates running pressure fluctuations downstream. In contrast to Refs. [17,19], the two critical angles θ_1 and θ_2 here are not symmetric with respect to the shock surface. That is, in general it is $\theta_2 \neq \pi - \theta_1$. This is because the upstream waves with $\theta < \pi/2$ have positive longitudinal velocities in the laboratory frame trying to escape from the shock, and the modes with $\theta > \pi/2$ move toward the shock, and hence their relative velocities are different. As a result, because of the Doppler shift, the value of $\zeta_{ac}(\theta)$ is different from $\zeta_{ac}(\pi - \theta)$, which also explains the difference between θ_1 and θ_2. These arguments do not apply to Refs. [17,19], as in those works the upstream modes are frozen to the fluid and the relative velocity of the modes oriented with θ and $\pi - \theta$ is exactly the same.

It is interesting to discuss the temporal transition of the shock perturbations toward the asymptotic regime. As previously commented, the poles of the Laplace transform at $s = \pm i\zeta_{ac}$ give rise to stable asymptotic oscillations, shown in Eqs. (40) and (41). In addition, the branch points at $s = \pm i$ are responsible of an asymptotic behavior similar to the asymptotic decay of Bessel functions. In fact, using Watson's lemma to study the asymptotic contribution of the branch points of $\tilde{P}_s(s)$ [27], we get the following trend for large times:

$$(\tilde{p}_s)_{\tau\gg 1} \cong \begin{cases} e_{l1}\cos\left(\zeta_{ac}\tau\sqrt{1-M_2^2}\right) + e_{l2}\sin\left(\zeta_{ac}\tau\sqrt{1-M_2^2}\right) \\ \quad + \left(\frac{\tau_c}{\tau}\right)^{3/2}\left[\cos\left(\tau\sqrt{1-M_2^2}\right) - \sin\left(\tau\sqrt{1-M_2^2}\right)\right] + O(\tau^{-5/2}), \quad |\zeta_{ac}| \leqslant 1, \\ e_s\cos\left(\zeta_{ac}\tau\sqrt{1-M_2^2}\right) \\ \quad + \left(\frac{\tau_c}{\tau}\right)^{3/2}\left[\cos\left(\tau\sqrt{1-M_2^2}\right) - \sin\left(\tau\sqrt{1-M_2^2}\right)\right] + O(\tau^{-5/2}), \quad |\zeta_{ac}| \geqslant 1, \end{cases} \tag{54}$$

where τ_c is a characteristic dimensionless time that describes the transition to the asymptotic stage. Its value is different for each branch:

$$\tau_c \cong \begin{cases} \frac{1}{\sqrt{1-M_2^2}}\left[\frac{\tilde{p}_{s0}2M_1^2M_2\left(M_1^2+2M_1M_2+1\right)\left(\zeta_{ac}^2-1\right)-4M_1^4M_2^2\alpha_{ac}}{\sqrt{\pi}\left(2M_1^2+1\right)^2\left(\zeta_{ac}^2-1\right)\sqrt{e_{l1}^2+e_{l2}^2}}\right]^{2/3}, & |\zeta_{ac}| \leqslant 1, \\ \frac{1}{\sqrt{1-M_2^2}}\left[\frac{\tilde{p}_{s0}2M_1^2M_2\left(M_1^2+2M_1M_2+1\right)\left(\zeta_{ac}^2-1\right)-4M_1^4M_2^2\alpha_{ac}}{\sqrt{\pi}\left(2M_1^2+1\right)^2\left(\zeta_{ac}^2-1\right)|e_s|}\right]^{2/3}, & |\zeta_{ac}| \geqslant 1. \end{cases} \tag{55}$$

We see that the characteristic time grows unbounded when the angle of incidence of the upstream sound wave is very close to any of the critical angles $|\zeta_{ac}| \cong 1$. This means that it takes longer for the shock perturbations to reach the asymptotic stable oscillations shown in Eq. (40) when $\theta \cong \theta_1, \theta_2$. Ideally, for an incidence angle exactly equal to the critical angle, an infinite time would be required to achieve the asymptotic stable oscillations of constant amplitude far downstream. This behavior may explain the difference observed in Fig. 2 of Ref. [10] between their numerical results and the linear theory.

C. Velocity perturbations generated downstream

As we can see from the RH Eqs. (13)–(16), the shock front generates velocity perturbations. In this section, we study the perturbed velocity at the weak surface discontinuity $x = 0$, the vorticity generated behind the shock, together with the corresponding rotational velocity field. Finally, the acoustic velocity field is studied. These results will be necessary for the calculation of the statistical averages of the different physical quantities in Sec. III.

1. Richtmyer-Meshkov growth at $x = 0$

As has been shown in Refs. [17,19], after the shock front enters the nonhomogeneous region, the weak surface discontinuity becomes RM unstable, even though the surface $x = 0$ is not a material surface separating different fluids. In fact, once the shock crosses it, vorticity is generated between the shock surface and the weak discontinuity. On the contrary, no vorticity is generated behind the neutrally stable sonic wave that gets reflected to the left at $t = 0^+$. As a consequence, the mathematical surface $x = 0$ gets rippled at $t = 0^+$, and it separates two different regions of the same fluid: rotational flow to the right and irrotational flow to the left of it. As the shock front progresses into the inhomogeneous fluid, pressure fluctuations fill the whole space downstream affecting the dynamics of the fluid elements at $x = 0$. In fact, the pressure perturbations emitted by the shock will modify the tangential velocity at the weak discontinuity, enhancing ripple growth in a manner similar to RM growth [15,24]. We can get the exact behavior of the weak discontinuity ripple as a function of time by using the Laplace transform of the fluid equations downstream, as has been already done in Refs. [17,19]. We take the Laplace transform of the x component of the Euler equation (13) with the aid of Eq. (45), evaluated at $\chi = 0$, and we get the function $\tilde{V}_{xi}$, the Laplace transform of the x component of the velocity at $x = 0$:

$$\tilde{V}_{xi} = \tilde{V}_x(\chi = 0, s) = -\frac{\cosh(\chi_s + \sinh^{-1} s)}{s} \times \tilde{P}_s(\chi_s + \sinh^{-1} s). \tag{56}$$

It can be rewritten as

$$\tilde{V}_{xi} = -\frac{\left[\left(M_2^2+1\right)s\sqrt{s^2+1} + 2M_2 s^2 + M_2\right]}{\left(M_2^2+1\right)s^2 + \left(1-M_2^2\right)\zeta_{\rm ac}^2 + M_2^2 + 2M_2 s\sqrt{s^2+1}} \frac{\beta_{00}\left[\left(M_2^2+1\right)s^2 + \left(1-M_2^2\right)\zeta_{\rm ac}^2 + M_2^2 + 2M_2 s\sqrt{s^2+1}\right] + \beta_{20}}{s(-\beta_{10}s^2 + s\sqrt{s^2+1} - \beta_{11})}, \tag{57}$$

where the coefficients β_{00}, β_{10}, β_{11}, and β_{20} are, respectively,

$$\begin{aligned}
\beta_{00} &= \frac{2M_1^2 M_2 + M_1^2 + 1}{M_2\left(2M_1^2M_2^2 + 4M_1^2 + 2\right)}\tilde{p}_{s0},\\
\beta_{10} &= -\frac{M_1^2\left(5M_2^2+1\right) + M_2^2 + 1}{2M_2\left[M_1^2\left(M_2^2+2\right)+1\right]},\\
\beta_{11} &= -\frac{M_1^2\left(2M_2^2+1\right) + M_2^2}{2M_2\left[M_1^2\left(M_2^2+2\right)+1\right]},\\
\beta_{20} &= -\frac{M_1^2\left(M_2^2-1\right)}{M_1^2\left(M_2^2+2\right)+1}\alpha_\sigma.
\end{aligned} \tag{58}$$

As we did before with the Laplace transform of the shock pressure perturbations, Eq. (35), the exact temporal evolution of the normal velocity at the weak discontinuity since $\tau = 0$ is formally given by [27]

$$\tilde{v}_{xi}(\tau) = \frac{1}{2\pi i}\int_{c-i\infty}^{c+i\infty} \tilde{V}_x(\chi = 0, s)\exp(s\,\tau)ds. \tag{59}$$

To compute the above expression, we proceed as has been done with Eq. (37). We recognize a pole at $s = 0$ that induces constant growth in time, given by the corresponding residue. The constant asymptotic velocity induced by the pole at $s = 0$ is [27]

$$\tilde{v}_{xi}^{\infty} = -\frac{\tilde{P}_s(s = \sinh\chi_s)}{\sqrt{1-M_2^2}} = -\frac{M_2\left(2M_1^2M_2 + M_1^2 + 1\right)\left[\left(1-M_2^2\right)\zeta_{\rm ac}^2 + M_2^2\right]\tilde{p}_{s0} + 2M_1^2\left(1-M_2^2\right)M_2^2\alpha_\sigma}{\left(2M_1^2M_2^2 + M_1^2 + M_2^2\right)\left[\left(1-M_2^2\right)\zeta_{\rm ac}^2 + M_2^2\right]}. \tag{60}$$

Besides, there is the possibility of a pole at $s = \pm i\zeta_1$, as happened in Eq. (14). In fact, the function $\tilde{P}_s(q + \chi_s)$ may give rise to running waves to the left, if $|\zeta_{\rm ac}| > 1/\sqrt{1-M_2^2}$. These acoustic waves induce an irrotational motion in the whole fluid downstream, affecting the weak discontinuity ripple, and making it oscillate with frequency ζ_1 superposed to the constant growth of Eq. (60). Summing up, the asymptotic behavior of the ripple at $x = 0$ can be described according to the value of $\zeta_{\rm ac}$ as

$$\tilde{v}_{xi}(\tau \gg 1) \cong \begin{cases} \tilde{v}_{xi}^{\infty}, & |\zeta_{\rm ac}| \leqslant \cosh(\chi_s), \\ \tilde{v}_{xi}^{\infty} + Q_{\rm ac}\cos(\zeta_1\tau), & |\zeta_{\rm ac}| \geqslant \cosh(\chi_s), \end{cases} \tag{61}$$

where the constant growth rate velocity $\tilde{v}_{xi}^{\infty}$ is given by Eq. (60) and the amplitude of the harmonic oscillations is given by the residues at the poles $s = \pm i\zeta_1$, in close analogy with [17,18]:

$$Q_{\rm ac} = \frac{M_2\zeta_{\rm ac} - \sqrt{\zeta_{\rm ac}^2 - 1}}{\zeta_{\rm ac} - M_2\sqrt{\zeta_{\rm ac}^2 - 1}}\, e_s. \tag{62}$$

There is an interesting fact regarding the formulas presented above for the RM growth at the surface $x = 0$. As seen in Fig. 3, the asymptotic linear velocity of the weak surface ripple is in general negative. In this sense, the growth resembles that of the RM instability at the contact surface separating different fluids for the case of a reflected rarefaction [28,29]. As a curiosity,

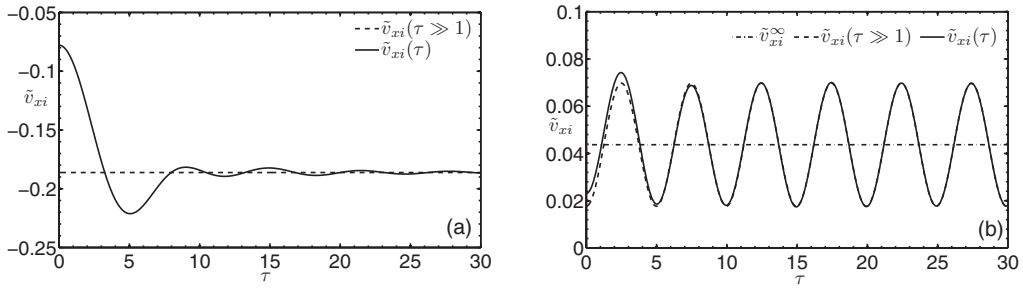

FIG. 3. Here we plot $\tilde{v}_{xi}$ for $M_1 = 2.0$ when $\gamma = 7/5$, and for an incident angle $\theta = \pi/4$, $\zeta_{ac} = 0.552\,285$ (a) and $\theta = \pi/6$, $\zeta_{ac} = 2.088\,61$ (b).

it can also be seen that the value of the asymptotic given by Eq. (60) can be made equal to zero for certain choices of the defining parameters γ, M_1, and θ. For example, if a shock wave with $M_1 = 2$ travels through an ideal gas with $\gamma = 7/5$ and the incoming acoustic wave is oriented through an angle $\theta \cong 29.503^\circ$ (which gives $\zeta_{ac} = 1.417\,96$), the growth rate $\tilde{v}_{xi}^{\infty}$ is exactly zero. We can also calculate the temporal evolution of the weak discontinuity ripple $\xi_i = k\psi_i(t)$. It can be obtained with the aid of Eq. (57) by means of the Laplace transform:

$$\xi_i(s) = \frac{\tilde{V}_{xi}}{s}. \tag{63}$$

The temporal evolution is calculated with the inverse Laplace transform:

$$\xi_i(\tau) = \frac{1}{2\pi i}\int_{c-i\infty}^{c+i\infty} \xi_i(s)\exp(s\,\tau)ds, \tag{64}$$

where c is any real number to the right of the singularities of $\tilde{V}_{xi}$. For the asymptotic behavior, we use the residues theorem and get

$$\xi_i(\tau \gg 1) \cong \begin{cases} \xi_{i0}^{\infty} + \tilde{v}_{xi}^{\infty}\tau, & \zeta_{ac} \leqslant \cosh(\chi_s), \\ \xi_{i0}^{\infty} + \tilde{v}_{xi}^{\infty}\tau + \frac{Q_{ac}}{\zeta_1}\sin(\zeta_1\tau), & \zeta_{ac} \geqslant \cosh(\chi_s). \end{cases} \tag{65}$$

It is noted that ξ_{i0}^{∞} is not zero, as is $\xi_i(\tau = 0^+)$. In fact, we get

$$\xi_{i0}^{\infty} = \tilde{p}_{s0}\frac{(M_2^2-1)(M_1^2-M_2^2)\left[M_1^2(2M_2+1)+1\right]}{\left[M_1^2(2M_2^2+1)+M_2^2\right]^2} + 2M_1^2M_2(M_2^2-1)\frac{M_1^2\left[M_2^4(\zeta_{ac}^2-5)-M_2^2(2\zeta_{ac}^2+1)+\zeta_{ac}^2\right]-M_2^6(\zeta_{ac}^2-1)+M_2^4(2\zeta_{ac}^2-3)-M_2^2\zeta_{ac}^2}{\left[M_1^2(2M_2^2+1)+M_2^2\right]^2\left[\zeta_{ac}^2-M_2^2(\zeta_{ac}^2-1)\right]^2}\alpha_\sigma. \tag{66}$$

2. *Vorticity generation downstream*

When the shock front moves through a perturbed flow its shape gets distorted, and to conserve the tangential momentum, tangential velocity is generated behind the shock. This mechanism is responsible for generating vorticity downstream. In the absence of viscosity, the vorticity field generated behind the shock remains frozen to the fluid particles, and the value at any point x corresponds to the vorticity deposited by the shock front at the time τ_0 at which the shock arrived at position "x": $\tau_0 = k_y x/M_2$. In a 2D geometry, the dimensionless vorticity vector behind the shock is formally defined as

$$\tilde{\vec{\omega}}_z = \frac{\vec{\omega}_z}{k_y c_2} = g(k_y x)\sin(k_y y)\hat{z}, \tag{67}$$

where the function g is actually given by

$$g(k_y x) = \frac{\partial}{\partial k_y x}\tilde{v}_y + \tilde{v}_x, \tag{68}$$

and it can be calculated using Eqs. (13)–(16) [17,19]:

$$g(k_y x_s) = \Omega_2\tilde{p}_s\left(\frac{\zeta_{ac}}{\sinh\chi_s}k_y x_s\right) - \Omega_4\cos\left(\frac{\zeta_{ac}}{\sinh\chi_s}k_y x_s\right). \tag{69}$$

The term $\Omega_2\tilde{p}_s$ is the vorticity contribution directly related to the shock curvature, and the second term $\Omega_4\cos(Rk_x x)$ takes into account the interaction between the zero-order shock pressure and density jumps with the upstream acoustic perturbation field. The missing coefficients Ω_1 and Ω_3 have been defined [18,19] to characterize the vorticity generation when a shock interacts with a vorticity and an entropy profile, respectively, and they are not present in the problem discussed here. The value of Ω_2 is equal to [17,19]

$$\Omega_2 = \frac{(M_1^2-1)^2\sqrt{2\gamma M_1^2-\gamma+1}}{M_1^2\left[(\gamma-1)M_1^2+2\right]^{3/2}}. \tag{70}$$

It can be seen that $\Omega_4 = -\Omega_2$, and therefore

$$g(k_y x) = \Omega_2\left[\tilde{p}_s\left(\frac{\zeta_{ac}}{\sinh\chi_s}k_y x\right) - \cos\left(\frac{\zeta_{ac}}{\sinh\chi_s}k_y x\right)\right]. \tag{71}$$

The above expression gives the exact vorticity deposition downstream at any value of the position x. We can calculate the spatial asymptotic of the vorticity field by evaluating the above expression at values of x far enough from the weak discontinuity and far from the shock surface.

We get

$$g(x \gg \lambda_y) \cong \begin{cases} \Omega_2\sqrt{e_{l1}^2+(e_{l2}-1)^2}\cos\left(\frac{\zeta_{\rm ac}}{\sinh\chi_s}k_y x+\phi_{\rm rot}\right), & |\zeta_{\rm ac}|\leqslant 1, \\ \Omega_2(e_s-1)\cos\left(\frac{\zeta_{\rm ac}}{\sinh\chi_s}k_y x\right), & |\zeta_{\rm ac}|\geqslant 1, \end{cases} \tag{72}$$

where $\phi_{\rm rot}$ is given by

$$\phi_{\rm rot}=\arctan\left(\frac{e_{l2}}{1-e_{l1}}\right). \tag{73}$$

3. Rotational velocity perturbations in the compressed fluid

The velocity perturbations can always be decomposed into rotational and irrotational contributions. The rotational perturbations are frozen to the fluid particles in the absence of viscosity and are associated with the vorticity calculated before. On the other hand, the acoustic perturbations are irrotational fluctuations that travel into the compressed fluid with the speed of sound. We thus make

$$\tilde{\vec{v}}(x,y,t)=\tilde{\vec{v}}_{\rm rot}(x,y)+\tilde{\vec{v}}_{\rm ac}(x,y,t). \tag{74}$$

After manipulating the fluid equations, it can be seen that the total velocity field downstream satisfies the differential equation:

$$\frac{\partial^2\tilde{\vec{v}}}{\partial\tau^2}=\vec{\nabla}_{\rm 2D}^2\tilde{\vec{v}}+\vec{\nabla}_{\rm 2D}\times(\vec{\nabla}_{\rm 2D}\times\tilde{\vec{v}}). \tag{75}$$

In this subsection, we focus only on the rotational part, and the previous differential equation becomes

$$\vec{\nabla}_{\rm 2D}^2\tilde{\vec{v}}_{\rm rot}=-\vec{\nabla}_{\rm 2D}\times(\vec{\nabla}_{\rm 2D}\times\tilde{\vec{v}}_{\rm rot}). \tag{76}$$

We define the longitudinal and transverse rotational components as

$$\begin{aligned} \tilde{v}_x^{\rm rot}(x,y)&=u(x)\cos(k_y y), \\ \tilde{v}_y^{\rm rot}(x,y)&=v(x)\sin(k_y y). \end{aligned} \tag{77}$$

As the rotational velocity field is incompressible, the relationship $v(x)=-u'(x)$ holds, where the prime indicates differentiation with respect to the argument. Using (68), (76), (77), and the incompressibility condition, it is easy to get the ordinary differential equations satisfied by u and v:

$$\frac{d^2u}{d(k_y x)^2}-u=-g(k_y x), \tag{78}$$

$$\frac{d^2v}{d(k_y x)^2}-v=g'(k_y x). \tag{79}$$

We concentrate on the solution of (76), as v is obtained from u by differentiation. The most general solution of (76) is written in the form

$$u(k_y x)=A\exp(-k_y x)+u_p(x), \tag{80}$$

where u_p is a particular solution and the constant A is chosen to match the value of the asymptotic velocity at $x=0$, given by Eq. (61). After some algebra, and using Eq. (38), a particular solution can be written as

$$\begin{aligned} u_p(k_y x)=&\frac{2\Omega_2\left(2M_2M_1^2-M_1^2-1\right)\tilde{p}_{s0}\sinh^2\chi_s}{\pi\left(2M_2M_1^2\right)} \\ &\times\int_0^1\left[\frac{f_p(z)}{z^2+\sinh^2\chi_s}\cos\left(\frac{k_y x}{\sinh\chi_s}z\right)\right]dz \\ &+\frac{\Omega_4\sinh^2\chi_s}{\sinh^2\chi_s+\zeta_{\rm ac}^2}\cos\left(\frac{k_y x}{\sinh\chi_s}\zeta_{\rm ac}\right) \\ &+\frac{2\Omega_2\alpha_\sigma}{\pi}\int_0^1\frac{f_p(z)j_u(z,x)}{\left(z^2-\zeta_{\rm ac}^2\right)}dz, \end{aligned} \tag{81}$$

where the auxiliary function j_u is

$$\begin{aligned} j_u(z,x)=&\frac{\sinh^2\chi_s}{\zeta_{\rm ac}^2+\sinh^2\chi_s}\cos\left(\frac{k_y x}{\sinh\chi_s}\zeta_{\rm ac}\right) \\ &-\frac{\sinh^2\chi_s}{z^2+\sinh^2\chi_s}\cos\left(\frac{k_y x}{\sinh\chi_s}z\right), \end{aligned} \tag{82}$$

and we note that the argument $\zeta_{\rm ac}k_y x/\sinh\chi_s$ is not equal to $Rk_x x$, as happened in Refs. [17,19] with $\zeta_0 k_y x/\sinh\chi_s$. From the arguments given above, it is clear that in order to match the velocity perturbation at $x=0$, we have the following expression for the asymptotic longitudinal velocity in the compressed fluid:

$$u(k_y x)=u_p(k_y x)-\tilde{v}_{xi}^{\infty}\exp(-k_y x). \tag{83}$$

The solution u_p is important very near the weak discontinuity surface $x=0$ and becomes negligible far away from it. The asymptotic expressions for the components of the rotational velocities are

$$\tilde{v}_x^{\rm rot}(x\gg\lambda_y,y) \cong \begin{cases} Q_{\rm rot}^l\cos\left(\frac{\zeta_{\rm ac}}{\sinh\chi_s}k_y x+\phi_{\rm rot}\right)\cos(k_y y), & |\zeta_{\rm ac}|\leqslant 1, \\ Q_{\rm rot}^s\cos\left(\frac{\zeta_{\rm ac}}{\sinh\chi_s}k_y x\right)\cos(k_y y), & |\zeta_{\rm ac}|\geqslant 1 \end{cases} \tag{84}$$

for the longitudinal component, and

$$\tilde{v}_y^{\rm rot}(x\gg\lambda_y,y) \cong \begin{cases} R\frac{k_x}{k_y}Q_{\rm rot}^l\sin\left(\frac{\zeta_{\rm ac}}{\sinh\chi_s}k_y x+\phi_{\rm rot}\right)\sin(k_y y), & |\zeta_{\rm ac}|\leqslant 1, \\ R\frac{k_x}{k_y}Q_{\rm rot}^s\sin\left(\frac{\zeta_{\rm ac}}{\sinh\chi_s}k_y x\right)\sin(k_y y), & |\zeta_{\rm ac}|\geqslant 1 \end{cases} \tag{85}$$

for the transverse component, where it is assumed that the point x is far enough from the interface $x=0$ and also that the shock front is far enough from x [that is, $x\ll(D-U)t$]. The quantities $Q_{\rm rot}^l$ and $Q_{\rm rot}^s$ are

$$Q_{\rm rot}^l=\frac{\Omega_2\sqrt{(e_{l1}-1)^2+e_{l2}^2}}{1+\left(\frac{\zeta_{\rm ac}}{\sinh\chi_s}\right)^2}, \tag{86}$$

$$Q_{\rm rot}^s=\frac{\Omega_2(e_s-1)}{1+\left(\frac{\zeta_{\rm ac}}{\sinh\chi_s}\right)^2}, \tag{87}$$

and $\phi_{\rm rot}$ is defined in Eq. (73).

4. Irrotational velocity perturbations downstream

The acoustic part of the velocity field satisfies the homogeneous wave equation:

$$\frac{\partial^2 \tilde{\vec{v}}_{\rm ac}}{\partial \tau^2} = \vec{\nabla}^2_{\rm 2D} \tilde{\vec{v}}_{\rm ac}. \tag{88}$$

When $|\zeta_{\rm ac}| < 1$, the solution to the previous equation is actually an evanescent sound wave that vanishes asymptotically in time like $t^{-3/2}$ at any position x behind the front. On the other hand, when $|\zeta_{\rm ac}| > 1/\sqrt{1-M_2^2}$, the solutions to Eq. (50) add an oscillating contribution to v_x, for $\tau \gg \tau_0(x)$, in the whole fluid downstream. These oscillations travel as planar fronts with a definite orientation in space toward $x = -\infty$. In fact, the function $\tilde{v}_x^{\rm ac}$ can be written, asymptotically in time, as

$$\tilde{v}_x^{\rm ac}(x \gg \lambda_y, y, \tau \gg \tau_0) = Q_{\rm ac} \cos\left(\zeta_1 \tau - k_x^{\rm ac} x\right) \cos\left(k_y y\right), \tag{89}$$

$$\tilde{v}_y^{\rm ac}(x \gg \lambda_y, y, \tau \gg \tau_0) = \frac{e_s}{\zeta_1} \sin\left(\zeta_1 \tau - k_x^{\rm ac} x\right) \sin\left(k_y y\right), \tag{90}$$

where $Q_{\rm ac}$ is given in Eq. (62).

D. Density perturbations generated downstream

The perturbed density field behind the shock front can be decomposed as the sum of entropic and acoustic contributions. In the absence of thermal conduction, the entropy nonuniformities remain frozen to the fluid particles, and the acoustic waves travel downstream as shown in the preceding subsection. We write

$$\tilde{\rho}(k_y x, \tau) = \tilde{\rho}_{\rm en}(k_y x) + \tilde{\rho}_{\rm ac}(k_y x, \tau). \tag{91}$$

The dimensionless acoustic fluctuation is given by Eq. (50):

$$\tilde{\rho}_{\rm ac}(k_y x, \tau) = \tilde{p}(k_y x, \tau), \tag{92}$$

and the entropic term can be obtained with the aid of Eq. (13) after subtracting the acoustic part:

$$\tilde{\rho}_{\rm en}(k_y x) = \left(\frac{1}{M_1^2 M_2^2} - 1\right) \tilde{p}_s \left(\frac{k_y x \sqrt{1-M_2^2}}{M_2}\right) + \left(1 - \frac{1}{M_1^2 M_2^2}\right) \frac{\delta\rho_1(k_y x)}{\rho_1}. \tag{93}$$

The asymptotic entropic density perturbations behind the corrugated shock front are thus

$$\tilde{\rho}_{\rm en}(x \gg \lambda_y) \cong \begin{cases} Q^l_{\rm en} \cos\left(\frac{\zeta_{\rm ac}}{\sinh \chi_s} k_y x + \phi_{\rm en}\right), & |\zeta_{\rm ac}| \leqslant 1, \\ Q^s_{\rm en} \cos\left(\frac{\zeta_{\rm ac}}{\sinh \chi_s} k_y x\right), & |\zeta_{\rm ac}| \geqslant 1, \end{cases} \tag{94}$$

where

$$Q^l_{\rm en} = \frac{\left(1 - M_1^2 M_2^2\right)}{M_1^2 M_2^2} \sqrt{(e_{l1} - 1)^2 + e_{l2}^2}, \tag{95}$$

$$Q^s_{\rm en} = \frac{\left(1 - M_1^2 M_2^2\right)}{M_1^2 M_2^2} (e_s - 1). \tag{96}$$

It can be seen that

$$\phi_{\rm en} = \phi_{\rm rot} = \arctan\left(\frac{e_{l2}}{1 - e_{l1}}\right). \tag{97}$$

We realize that there is no shift between the vorticity and the entropy modes downstream, as opposed to the situation found in shock/vorticity [17] and shock/entropy [19] interactions. In the case studied here, there is no vorticity and entropy ahead of the shock front, and hence there is no shift in the spatial distributions of vorticity or entropy perturbations downstream.

E. Acoustic flux

The short-wavelength modes induce downstream sound emission in the form of running sonic waves. Therefore, acoustic energy is continuously radiated downstream. In order to calculate the emitted energy flux, we proceed similarly as in Refs. [17,19]. Let us denote the energy flux by $\vec{q}$, which in the compressed fluid system of reference is equal to [30]

$$\vec{q} = c_2 E \vec{k}_{\rm ac}, \tag{98}$$

and the energy density E is given by

$$E = \rho_2 c_2^3 \tilde{p}^2. \tag{99}$$

The value of $\tilde{p}$ above is given by the asymptotic expression for the pressure field downstream. In addition, with the help of Eq. (50), we get the components of the vector $\vec{k}_{\rm ac}$ downstream. We note that the intervals $\zeta_{\rm ac} \geqslant 1$ and $\zeta_{\rm ac} \leqslant -1$ give different results. This is a consequence of the fact that upstream waves with $\theta < \theta_1$ induce shock oscillations with frequencies different from the upstream waves impinging on the shock surface with $\theta > \theta_2$. Mathematically, this is represented by the fact that the positive square root determination is to be used for $\theta < \theta_1$ and the negative determination for $\theta > \theta_2$. We have

$$\vec{k}_{\rm ac} = \frac{k_x^{\rm ac} \hat{x} + k_y \hat{y}}{\sqrt{\left(k_x^{\rm ac}\right)^2 + k_y^2}} = (\cos\theta_{\rm ac}, \sin\theta_{\rm ac}, 0) = \begin{cases} \left(\frac{M_2\zeta_{\rm ac} - \sqrt{\zeta_{\rm ac}^2 - 1}}{\zeta_{\rm ac} - M_2\sqrt{\zeta_{\rm ac}^2 - 1}}, \frac{\sqrt{1-M_2^2}}{\zeta_{\rm ac} - M_2\sqrt{\zeta_{\rm ac}^2 - 1}}, 0\right), & \zeta_{\rm ac} \geqslant 1, \\ \left(\frac{M_2\zeta_{\rm ac} + \sqrt{\zeta_{\rm ac}^2 - 1}}{\zeta_{\rm ac} + M_2\sqrt{\zeta_{\rm ac}^2 - 1}}, \frac{-\sqrt{1-M_2^2}}{\zeta_{\rm ac} + M_2\sqrt{\zeta_{\rm ac}^2 - 1}}, 0\right), & \zeta_{\rm ac} \leqslant -1. \end{cases} \tag{100}$$

As in some experiments the shock front remains steady with respect to the laboratory walls and the gas upstream is convected toward the shock, it is convenient to analyze the emitted acoustic flux in the system of reference in which the shock is at rest. It is clear that in the shock system of reference, all the sound waves with $|\zeta_{\rm ac}| > 1$ escape from the shock to the left. Nevertheless, due to the change of the system of reference, the direction of propagation of energy by the sonic wave does not coincide with $\vec{k}_{\rm ac}$. In fact, the energy flux is rewritten now as

$$\vec{q} = \vec{v}_{\rm ac} E_s, \tag{101}$$

in which $\vec{v}_{\rm ac} = c_2 \hat{k} + (U - D)\hat{x}$ and E_s is the energy density in the shock system of reference. Following [30], we write

$$E_s = (M_2 - \cos\theta_{\rm ac}) E. \tag{102}$$

The average of the above expression (101) over the angle ϕ on the shock surface gives, in units of $\rho_2 c_2^3$,

$$\langle \tilde{q}_x \rangle_\phi = \frac{\langle q_x \rangle_\phi}{\rho_2 c_2^3} = \frac{e_s^2}{2}(1 - M_2 \cos\theta_{\rm ac})(M_2 - \cos\theta_{\rm ac}). \quad (103)$$

Even though the expression for the flux remains formally similar to the acoustic fluxes studied in Refs. [17,19] for the cases of preshock vorticity and preshock entropy, as functions of $\zeta_{\rm ac}$ or ζ_0, there is an intrinsic difference here with regard to the orientation of the incident acoustic front upstream (except for very strong shocks, as discussed at the end of this subsection). In Refs. [17,19], both intervals $\zeta_0 \geqslant 1$ and $\zeta_0 \leqslant -1$ were symmetrical and generated the same pattern of acoustic intensity radiated downstream. For the case of a field of incident sound waves upstream, both intervals are no longer symmetrical. This is due to the difference in the relative velocities of the sonic fronts that have $\theta < \theta_1$ and the sonic waves that have $\theta > \theta_2$. This asymmetry makes it interesting to study the behavior of the averaged acoustic flux as a function of the angle θ' that the emitted sonic wave downstream forms with the x axis in the shock reference frame, as there will be two branches that will not be coincident, as happened in Refs. [17,18]. Before doing that, we need an expression of θ' as a function of $\theta_{\rm ac}$. After some algebra, we get the following expression:

$$\cos\theta' = \frac{\cos\theta_{\rm ac} - M_2}{\sqrt{1 + M_2^2 - 2M_2\cos\theta_{\rm ac}}}. \quad (104)$$

By direct substitution, we see that for $|\zeta_{\rm ac}| = 1$, it is $\cos\theta_{\rm ac} = M_2$ and hence $\theta' = \pi/2$. This means that, in the limit between stable or evanescent acoustic emission $|\zeta_{\rm ac}| = 1$, the sound waves emitted downstream point vertically in the shock wave reference frame. On the other hand, for $|\zeta_{\rm ac}| = \infty$, it is $\cos\theta_{\rm ac} = \pi$ and hence $\theta' = \pi$, therefore all sound waves emitted by the shock front point horizontally backward [we refer to the discussion after Eq. (52)]. We plot in Fig. 4 the dimensionless acoustic energy flux $\langle \tilde{q}_x \rangle_\phi$ as a function of the emission angle θ' in order to study in which directions the acoustic energy flux radiated by the shock is more important. In Figs. 4(a) and 4(b), we show it for a shock moving into air with shock Mach numbers $M_1 = 5$ and 50. We notice that the emission induced by the upstream waves pointing toward the shock front is greater by an order of magnitude in this case. This difference is even more accentuated for shocks that have weak to moderate strengths. For very strong shocks, however, the difference between the two types of orientations upstream disappears. In fact, for a very supersonic shock, there is almost no appreciable difference between $D - c_1$ and $D + c_1$, and as a consequence the pattern of acoustic downstream emission is almost the same in both intervals. Furthermore, the polar emission pattern of Fig. 4(b) resembles the same behavior of Fig. 12 in Ref. [19] for correspondingly stronger shocks.

It is also interesting to analyze the same trends for a very compressible gas with $\gamma = 1$. For a shock moving into a highly compressible fluid, the downstream polar emission pattern shows the behavior shown in Figs. 4(c) and 4(d) for two values of the incident shock strength ($M_1 = 5{,}50$). For weak to moderate shocks, both intervals are clearly asymmetric and the more intense branch shows a peak of emission in a direction nearly perpendicular to the shock surface. As the shock strength increases, both branches equalize the intensity of the emitted sound, and the shape of both curves tends to that of a circle of radius unity. The more intense emission is observed for $\theta' = \pi$, which corresponds to both $\zeta_{\rm ac} = \pm\infty$. This behavior is in contrast to that observed in Ref. [17], where the acoustic emission normal to the shock was zero at any shock intensity for the shock/vorticity interaction [17].

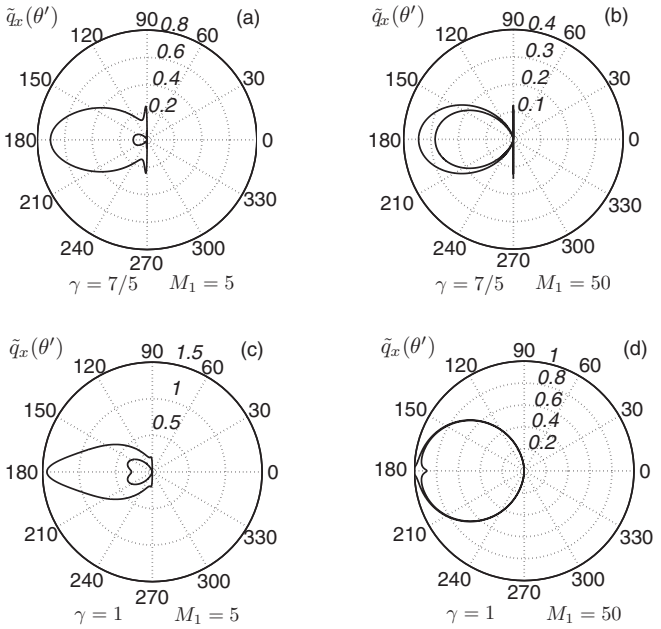

FIG. 4. Polar plots of the dimensionless acoustic energy flux $\langle \tilde{q}_x \rangle_\phi$ as a function of the emission angle θ' in the shock wave reference frame for different values of adiabatic index $\gamma = 7/5, 1$ and shock strengths $M_1 = 5{,}50$. The inner curve in each plot corresponds to the downstream acoustic energy flux generated by the upstream sonic waves traveling to the right. The outer curves are related to the upstream sound waves traveling to the left impinging on the shock front.

III. SHOCK WAVE TRAVELING INTO A RANDOM ISOTROPIC ACOUSTIC FIELD

We study now the interaction of a planar shock wave with a full spectrum of sound waves isotropically distributed in two and three dimensions. We assume that the upstream modes are uncorrelated. The statistical averages of the quantities downstream are then easily calculated by assuming a uniform distribution of the wave-number vectors in the corresponding space, as has been done in Refs. [5,17,19]. That is, for a 2D spectrum, we assume that the probability of finding a sound wave oriented with the angle θ is equal to $d\theta/\pi$, which means that the tips of the wave-number vectors are uniformly distributed over the unit semicircle in the (k_x, k_y) plane. On the other hand, for a 3D isotropic spectrum, we assume that the tips of the vectors (k_x, k_y, k_z) are uniformly distributed over the unit sphere in the 3D (k_x, k_y, k_z) space, and hence the probability of finding a wave-number vector oriented according to the angles θ and φ (polar angle on the shock surface) is proportional to $\sin\theta\, d\theta\, d\varphi$. In the following subsections, we present the statistical averages for the kinetic energy, acoustic energy flux, vorticity, and density, both in two and three dimensions, and

we show the limiting expressions obtained in the important limits of very weak and strong shocks as well as for highly compressible fluids. To this end, we use the 2D single-mode theory developed in the previous section for both 2D and 3D problems. By proper rotation of the coordinate axis on the shock surface, we can always reduce the 3D problem to an equivalent 2D problem. The z axis on the shock surface can always be rotated in such a way as to make $k_z = 0$ for any upstream mode. Hence, in the rotated system, the shock ripple does not depend on the z coordinate, and therefore no velocity perturbation is generated along that direction. Therefore, a 3D upstream spectrum can always be handled with the 2D model developed before. This trick has been extensively used in previous works [9,10,17,19].

A. Downstream kinetic energy

Once the shock has entered the half-space $x > 0$, filled with running sound waves, the shock surface gets rippled and oscillates in time, generating pressure and velocity fluctuations downstream. Part of these velocity perturbations are rotational as they are associated with the vorticity field that has been calculated in the preceding section. The amplitudes of the x and y components of the downstream rotational velocity field are given in Eqs. (82)–(85). The statistical average of the downstream rotational kinetic energy per unit mass is formally written as

$$K_{\rm rot} = \int \left[\left(\tilde{v}_x^{\rm rot}\right)^2 + \left(\tilde{v}_y^{\rm rot}\right)^2\right] dP(\theta,\phi), \tag{105}$$

where $dP(\theta,\phi)$ is the probability density function that describes the distribution of the wave-number vectors over the upstream spectrum. As discussed before, we distinguish between isotropic 2D and 3D spectra. The corresponding probability densities are

$$\begin{aligned} dP_{\rm 2D} &= \frac{1}{\pi} d\theta, \\ dP_{\rm 3D} &= \frac{1}{2} \sin\theta \, d\theta, \end{aligned} \tag{106}$$

where, thanks to isotropy condition, we assume rotational symmetry in φ for the 3D case. As shown in the preceding section, all the quantities downstream can be expressed as functions of $\zeta_{\rm ac}$. Therefore, it is convenient also to express the probability densities in terms of $\zeta_{\rm ac}$ for both two and three dimensions. That is, we can write

$$dP_{\rm 2D/3D} = J_{\rm 2D/3D}(\zeta_{\rm ac}) d\zeta_{\rm ac}, \tag{107}$$

where the functions $J_{\rm 2D/3D}$ are obtained working out the expressions given in Eqs. (26)–(28):

$$\begin{aligned} J_{\rm 2D}(\zeta_{\rm ac}) &= -\frac{2\left(M_1^2-1\right)M_2}{\pi M_1 \sqrt{1-M_2^2}} \frac{\sin^2\theta}{\cos\theta - M_1}, \\ J_{\rm 3D}(\zeta_{\rm ac}) &= -\frac{\left(M_1^2-1\right)M_2}{M_1 \sqrt{1-M_2^2}} \frac{\sin^3\theta}{\cos\theta - M_1}. \end{aligned} \tag{108}$$

The incident angle θ is considered a function of $\zeta_{\rm ac}$ using both Eqs. (27) and (28). For arbitrary values of γ and M_1, the probability densities either in two or three dimensions are asymmetric functions of $\zeta_{\rm ac}$ with respect to the axis $\zeta_{\rm ac} = 0$. For very strong shocks, they are completely symmetric and agree with the same functions used in the preshock density problem [see Eqs. (65) and (127) of [19]]. As the asymptotic behavior depends on the value of $\zeta_{\rm ac}$, we split the integrals that define the statistical averages in long- ($|\zeta_{\rm ac}| < 1$) and short-wavelength ($|\zeta_{\rm ac}| > 1$) contributions. For the averages of the rotational kinetic energies in two and three dimensions, we deduce, for the long-wavelength branch,

$$\begin{aligned} K_{\rm 2D}^{l} &= \frac{1}{2}\int_{-1}^{1} \left(1 + \frac{\zeta_{\rm ac}^2}{\sinh^2\chi_s}\right) \left|Q_l^{\rm rot}\right|^2 J_{\rm 2D}(\zeta_{\rm ac}) d\zeta_{\rm ac}, \\ K_{\rm 3D}^{l} &= \frac{1}{2}\int_{-1}^{1} \left(1 + \frac{\zeta_{\rm ac}^2}{\sinh^2\chi_s}\right) \left|Q_l^{\rm rot}\right|^2 J_{\rm 3D}(\zeta_{\rm ac}) d\zeta_{\rm ac}, \end{aligned} \tag{109}$$

and for the short-wavelength interval,

$$\begin{aligned} K_{\rm 2D}^{s} &= \frac{1}{2}\int_{-\infty}^{-1} \left(1 + \frac{\zeta_{\rm ac}^2}{\sinh^2\chi_s}\right) \left|Q_s^{\rm rot}\right|^2 J_{\rm 2D}(\zeta_{\rm ac}) d\zeta_{\rm ac} \\ &\quad + \frac{1}{2}\int_{1}^{\infty} \left(1 + \frac{\zeta_{\rm ac}^2}{\sinh^2\chi_s}\right) \left|Q_s^{\rm rot}\right|^2 J_{\rm 2D}(\zeta_{\rm ac}) d\zeta_{\rm ac}, \\ K_{\rm 3D}^{s} &= \frac{1}{2}\int_{-\infty}^{-1} \left(1 + \frac{\zeta_{\rm ac}^2}{\sinh^2\chi_s}\right) \left|Q_s^{\rm rot}\right|^2 J_{\rm 3D}(\zeta_{\rm ac}) d\zeta_{\rm ac} \\ &\quad + \frac{1}{2}\int_{1}^{\infty} \left(1 + \frac{\zeta_{\rm ac}^2}{\sinh^2\chi_s}\right) \left|Q_s^{\rm rot}\right|^2 J_{\rm 3D}(\zeta_{\rm ac}) d\zeta_{\rm ac}. \end{aligned} \tag{110}$$

We also calculate the acoustic kinetic energy generated downstream. The averaged acoustic contribution to the turbulent kinetic energy downstream is formally given by

$$\begin{aligned} K_{\rm 2D}^{\rm ac} &= \frac{1}{2}\int_{-\infty}^{-1} e_s^2 \, J_{\rm 2D}(\zeta_{\rm ac}) d\zeta_{\rm ac} + \frac{1}{2}\int_{1}^{\infty} e_s^2 \, J_{\rm 2D}(\zeta_{\rm ac}) d\zeta_{\rm ac}, \\ K_{\rm 3D}^{\rm ac} &= \frac{1}{2}\int_{-\infty}^{-1} e_s^2 \, J_{\rm 3D}(\zeta_{\rm ac}) d\zeta_{\rm ac} + \frac{1}{2}\int_{1}^{\infty} e_s^2 \, J_{\rm 3D}(\zeta_{\rm ac}) d\zeta_{\rm ac}, \end{aligned} \tag{111}$$

where only modes with $|\zeta_{\rm ac}| > 1$ are considered, and the value of e_s is given in Eq. (41). In Fig. 5, we show the different components for the kinetic energy amplification compared with the results shown by Mahesh *et al.* in Fig. 8 of [10]. Care must be taken with the different normalization of the upstream velocities. In Eq. (5) we have used c_1, while c_2 is used in Ref. [10].

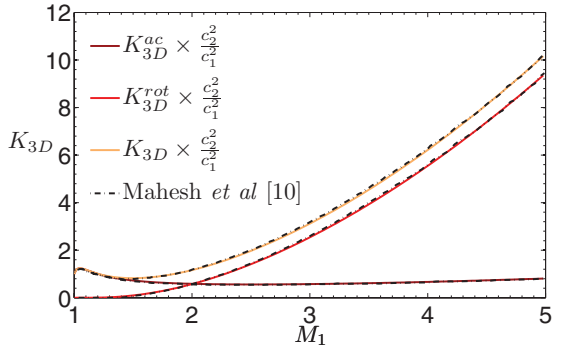

FIG. 5. (Color online) 3D kinetic energy contributions as a function of the shock strength M_1 and for $\gamma = 7/5$, superposed with the results shown in Fig. 8 of [10].

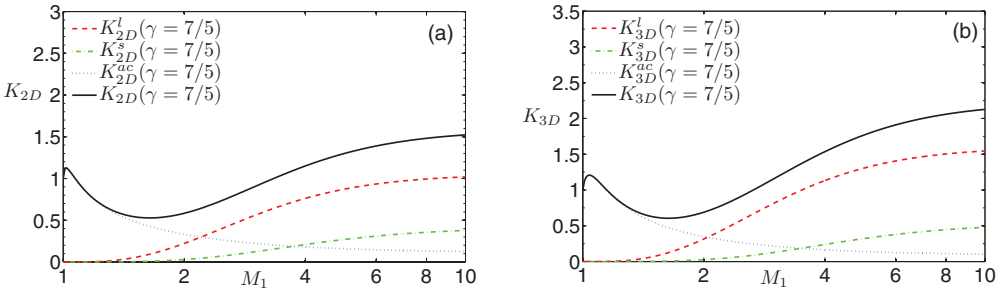

FIG. 6. (Color online) 2D and 3D kinetic energy contributions as a function of the shock strength M_1 and for $\gamma = 7/5$.

Therefore, the kinetic energy amplification obtained here, K_{3D}, is related with their corresponding parameter q^2 as follows: $q^2 \times c_1^2 = K_{3D} \times c_2^2$. In Fig. 5, we observe a perfect agreement between the different contributions to the kinetic energy given by Eqs. (109)–(111) and the results shown in Ref. [10]. In Figs. 6(a) and 6(b), we show the different contributions of the averaged total kinetic energy as a function of the shock strength for a shock moving into air. We notice that for weak shocks, the acoustic contribution is dominant, but for strong shocks the rotational part becomes more important, as also noticed in Ref. [10]. Both K_{2D} and K_{3D} look quite similar, and the differences between them reside in an overall scaling factor. The acoustic contribution rises rapidly for very weak shocks and later reaches an asymptotic limit that depends on γ. The rotational contribution also approaches an asymptotic value for the very strong shocks that depends on γ. For the shock moving in air, K^{ac}_{2D} tends to 0.111 612 when $M_1 \gg 1$, and the 3D value is 0.085 96. The total turbulent kinetic energy value for very strong shocks into air is equal to 1.569 05 in two dimensions and 2.2138 in three dimensions. In Fig. 7, we show the behavior of K^{ac}_{2D} and K^{ac}_{3D} as a function of γ and M_1. We observe that for very weak shocks ($M_1 - 1 \ll 1$), the amplification factor does not depend on the gas compressibility γ. On the other hand, it can also be seen that the acoustic kinetic energy decreases for gases with low compressibility. In Fig. 8, we show the behavior of the 2D and 3D downstream total kinetic energy ($K_{2D/3D} = K^l_{2D/3D} + K^s_{2D/3D} + K^{ac}_{2D/3D}$) as a function of γ and M_1. From both figures [Figs. 8(a) and 8(b), or posteriorly in Figs. 10(a) and 10(b)], we notice that the turbulent kinetic energy grows unbounded in highly compressible gases ($\gamma = 1$). In real gases, where viscosity and thermal conduction effects are taken into account, the kinetic energy will be bounded in that limit. As can be inferred from the previous figures, the turbulent kinetic energy is bounded for strong shocks, except perhaps in the highly compressible limit. Making adequate Taylor series expansions of the defining integrals, we can study the exact asymptotic behavior of the statistical averages downstream in the important physical limits of strong shock ($M_1 \gg 1$) and highly compressible fluid ($\gamma - 1 \ll 1$). We show in Appendix B the different components of those expressions in three dimensions. For the strong shock limit, we refer to Eqs. (B1)–(B4), and for $\gamma - 1 \ll 1$ we refer to Eqs. (B5)–(B8). The strong shock limit for the total turbulent kinetic energy Eq. (B4) can be further simplified in the limits $\gamma - 1 \ll 1$ or $\gamma \gg 1$:

$$K_{3D}(\gamma, M_1 \gg 1) \cong \begin{cases} \sqrt{\frac{2}{\gamma-1}}\left[\ln\left(\frac{2}{\gamma-1}\right) - 1\right] + \pi - 1 + O[(\gamma-1)^{1/2}], & \gamma - 1 \ll 1, \\ \frac{29-6\sqrt{2}}{15}\frac{1}{\gamma^2} + O\left(\frac{1}{\gamma^{5/2}}\right), & \gamma \gg 1. \end{cases} \tag{112}$$

In Figs. 9(b) and 10(b), we compare the above formulas shown in the strong shock limit together with $M_1 = 5$ and 10 shocks. The corresponding 2D plots are also shown in Figs. 9(a) and 10(a) for completeness, even though the corresponding asymptotic formulas are not shown. We remark here again that in the strong shock limit, the interaction of a shock with an isotropic field of acoustic waves gives the same results as the interaction with an isotropic field of density/entropy perturbations, as discussed in the preceding section. This can be confirmed by comparing the equations above in the limit $M_1 \gg 1$ with the corresponding formulas for the preshock entropy problem [see Eqs. (130)–(134) of [19]]. For a very strong shock, the nonadiabaticity of the upstream perturbations is irrelevant as far as downstream perturbation generation is concerned. In Fig. 11, we plot the acoustic contribution for highly compressible gases and also for $\gamma = 1.01$ and 1.1, either in two or three dimensions as a function of the shock strength. We observe that for weak shocks, all the curves are coincident because there is no γ dependence in that limit. In Fig. 12, we plot the total kinetic energy amplification K_{2D} and K_{3D} in the limit $\gamma - 1 \ll 1$. As we deduce from Fig. 10, the curve is unbounded when $\gamma \to 1$. The highly compressible gases limit Eq. (B8) can still be simplified in the limits $M_1 - 1 \ll 1$ and $M_1 \gg 1$:

$$K_{3D}(\gamma - 1 \ll 1, M_1) \cong \begin{cases} 1 + \frac{82+196\sqrt{2}-120\ln 2}{30}(M_1 - 1) + O[(M_1-1)^2], & M_1 - 1 \ll 1, \\ 2M_1 \ln M_1 + M_1\left(\ln 4 - \frac{5}{3}\right) + \pi - \frac{1}{3} + O\left(\frac{1}{M_1}\right), & M_1 \gg 1. \end{cases} \tag{113}$$

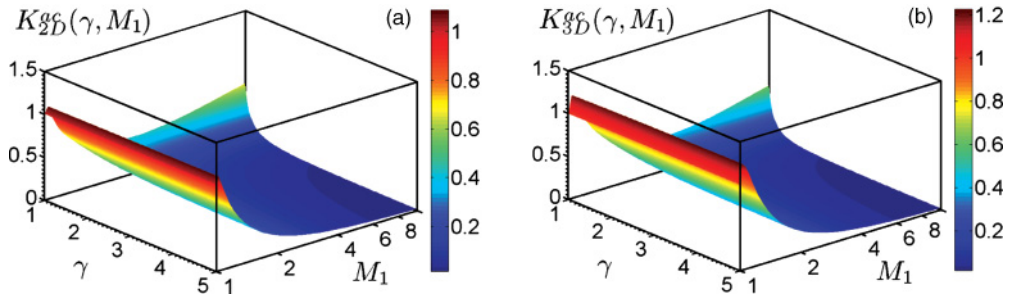

FIG. 7. (Color online) $K^{\rm ac}_{\rm 2D}$ and $K^{\rm ac}_{\rm 3D}$ as a function of the shock strength M_1 and γ.

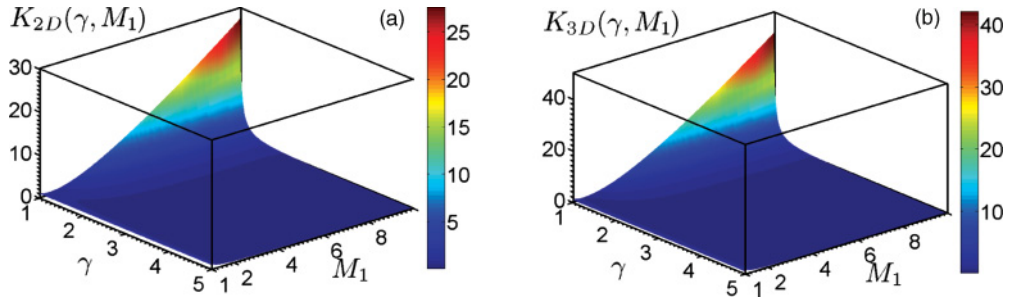

FIG. 8. (Color online) $K_{\rm 2D}$ and $K_{\rm 3D}$ as a function of the shock strength M_1 and γ.

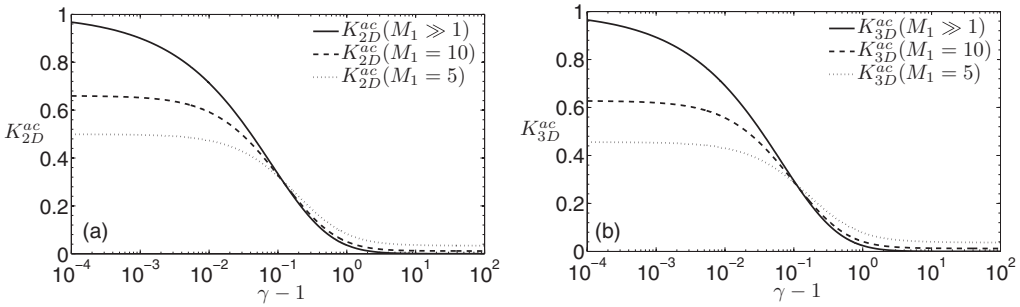

FIG. 9. $K^{\rm ac}_{\rm 2D}$ and $K^{\rm ac}_{\rm 3D}$ in the strong shock limit, and also for some finite values of the Mach number as a function of γ.

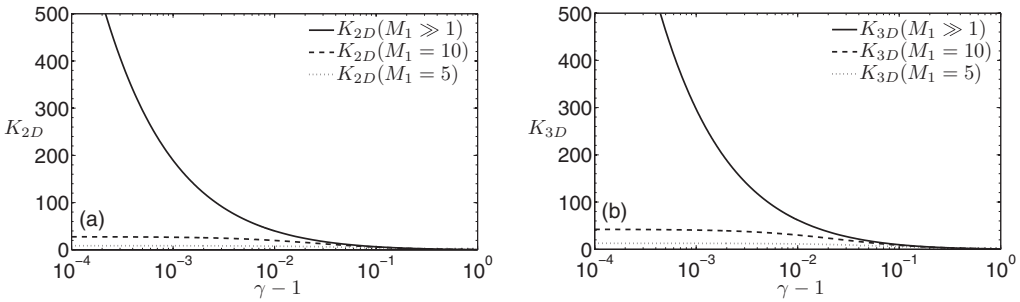

FIG. 10. $K_{\rm 2D}$ and $K_{\rm 3D}$ in the strong shock limit, and also for some finite values of the Mach number as a function of γ.

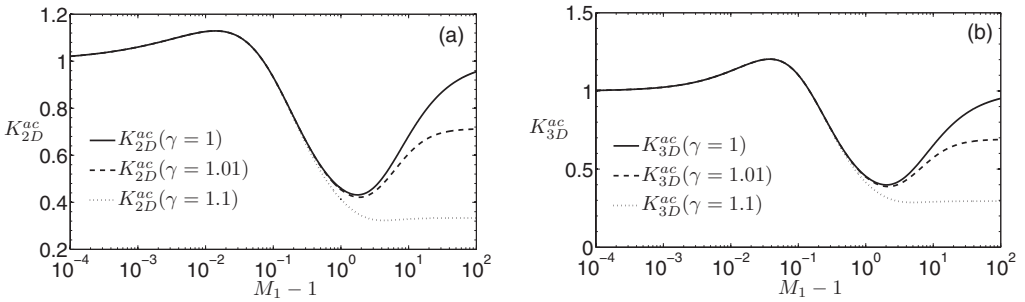

FIG. 11. K_{2D}^{ac} and K_{3D}^{ac} in the high compressibility limit ($\gamma - 1 \ll 1$), and also for some low values of γ as a function of the shock strength M_1.

We notice that the strong shock scaling in the above formula is the same ($\sim M_1 \ln M_1^2$) as the strong shock scaling observed in the highly compressible limit of the problem studied in Ref. [19], in agreement with the previous discussion. The weak shock limit for arbitrary values of γ is dominated by the acoustic contribution:

$$K_{3D}(\gamma, M_1 - 1 \ll 1) \cong 1 + \frac{98\sqrt{2} - 191}{15}(M_1 - 1) - 4(M_1 - 1) \times \ln(M_1 - 1) + O[(M_1 - 1)^2]. \quad (114)$$

B. Acoustic flux

We calculate the average of the acoustic flux radiated downstream in a system that moves with the shock front. In the same way as was done in previous works [17,19], we define the average intensity downstream as the angle average of the expression given by Eq. (103),

$$I_{3D}^{ac} = \langle q_x \rangle_{\phi,\theta} = \frac{\rho_2 c_2^3 \sigma_k^2}{2} \int_0^{\theta_1} e_s^2 (1 - M_2 \cos\theta_{ac}) \times (M_2 - \cos\theta_{ac}) \sin\theta \, d\theta + \frac{\rho_2 c_2^3}{2} \int_{\theta_2}^{\pi} e_s^2 \times (1 - M_2 \cos\theta_{ac})(M_2 - \cos\theta_{ac}) \sin\theta \, d\theta. \quad (115)$$

We normalize the above intensity with the average acoustic intensity incident on the shock upstream. It is calculated using the same formulas as above, where M_2 is substituted by M_1:

$$I_{3D}^{inc} = \frac{\rho_1 c_1^3}{2} \sigma_k^2 \int_0^{\pi} (1 - M_1 \cos\theta) \times (M_1 - \cos\theta) \sin\theta \, d\theta = \frac{4M_1}{3} \rho_1 c_1^3. \quad (116)$$

In two dimensions, the average acoustic intensity flux is

$$I_{2D}^{inc} = \frac{2}{\pi} \frac{\rho_1 c_1^3}{2} \sigma_k^2 \int_0^{\pi} (1 - M_1 \cos\theta) \times (M_1 - \cos\theta) \, d\theta = 3 M_1 \rho_1 c_1^3. \quad (117)$$

The relative acoustic flux downstream is defined as

$$S_{2D/3D} = \frac{I_{2D/3D}^{ac}}{I_{2D/3D}^{inc}}. \quad (118)$$

In Figs. 13(a) and 13(b), we show the acoustic energy flux as a function of the shock strength for a shock moving into air. In Fig. 14, we show the behavior of S_{2D} and S_{3D} as a function of γ and M_1. By making a Taylor expansion, as with the turbulent kinetic energy, it can be seen that for very strong shocks, the relative acoustic flux grows proportional to M_1^2. In the limit $M_1 \gg 1$, we get Eq. (B9). If we compare Eq. (B9) with Eq. (142) in Ref. [19], we find the following relationship: $S_{3D}(\gamma, M_1 \gg 1) = (3/8) M_1^2 \times S_{3D}(\gamma, M_1 \gg 1)$. In addition, for the 2D case [Eq. (94) in Ref. [19]], it can be deduced that $S_{2D}(\gamma, M_1 \gg 1) = 3M_1^2 \times S_{2D}(\gamma, M_1 \gg 1)$. Equation (B9) can be simplified in the limits of highly compressible and highly incompressible

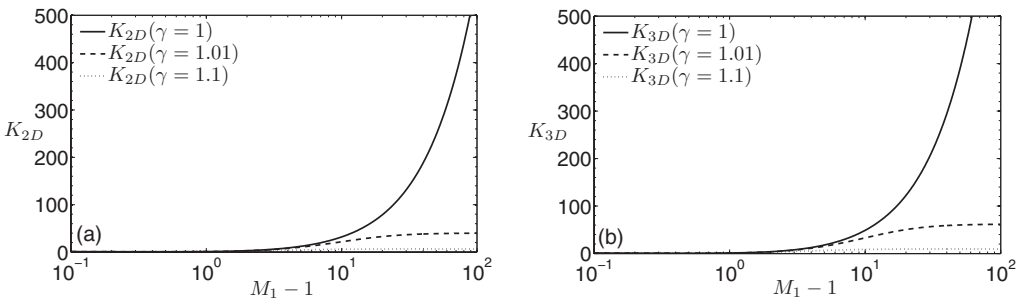

FIG. 12. K_{2D} and K_{3D} in the high compressibility limit ($\gamma = 1$), and also for some low values of γ as a function of the shock strength M_1.

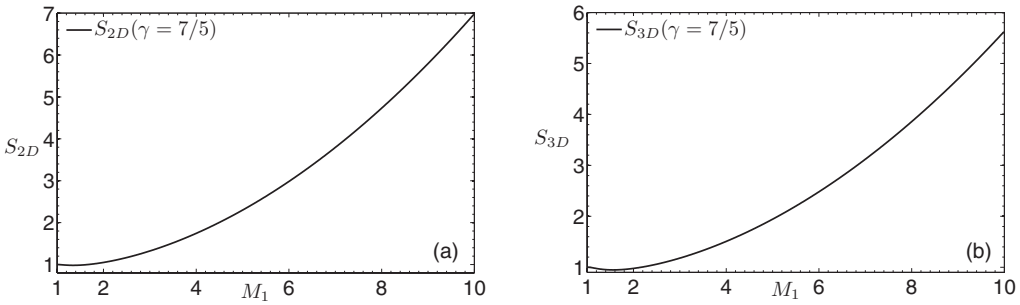

FIG. 13. 2D and 3D acoustic energy flux as a function of the shock strength M_1 and for $\gamma = 7/5$.

fluids:

$$S_{3D}(\gamma, M_1 \gg 1) \cong \begin{cases} \left\{\frac{3}{4\sqrt{2}}\sqrt{\gamma-1} - \frac{3}{4}(\gamma-1) + O[(\gamma-1)^{3/2}]\right\} M_1^2 + O(M_1), & \gamma - 1 \ll 1, \\ \left[\frac{3}{20\sqrt{2}}\frac{1}{\gamma^3} + \left(\frac{17}{40\sqrt{2}} - \frac{11}{35}\right)\frac{1}{\gamma^3} + O\left(\frac{1}{\gamma^4}\right)\right] M_1^2 + O(M_1), & \gamma \gg 1. \end{cases} \tag{119}$$

It is interesting to compare the function S_{2D}/M_1^2 and S_{3D}/M_1^2 in the strong shock limit with the same function at other finite values of the shock strength ($M_1 = 5, 10$). We show this comparison in Fig. 15(b). We observe a maximum of $S_{2D}(M_1 \gg 1)/M_1^2 \cong 0.0726$ at $\gamma = 1.152$ in two dimensions and a maximum value of $S_{3D}(M_1 \gg 1)/M_1^2 \cong 0.067\,433\,7$ at $\gamma = 1.102\,81$ in three dimensions. On the other hand, the acoustic energy flux is expressed as a function of M_1 for highly compressible gases in Eq. (B10), which can be further simplified in the weak and strong shock limits as

$$S_{3D}(\gamma - 1 \ll 1, M_1) \cong \begin{cases} 1 - \frac{7(64\sqrt{2}-33)}{20}(M_1-1)^3 + O[(M_1-1)^4], & M_1 - 1 \ll 1, \\ \frac{3M_1}{4} - \frac{3(4+\pi)}{8} + \frac{11}{2M_1} + O\left(\frac{1}{M_1^2}\right), & M_1 \gg 1. \end{cases} \tag{120}$$

Figure 16 shows the acoustic energy flux in the highly compressible gases limit, together with the acoustic flux at other values of the adiabatic index ($\gamma = 1.01, 1.1$). Finally, we show next the scaling for very weak shocks at arbitrary values of γ:

$$S_{3D}(\gamma, M_1 - 1 \ll 1) \cong 1 - \frac{7(64\sqrt{2}-33)}{20}(M_1-1)^3 + O[(M_1-1)^4], \tag{121}$$

where we realize the same trend as the acoustic kinetic energy in that limit, that is, no dependence on γ at the leading order.

C. Downstream vorticity generation

When the shock enters the nonuniform region, its shape gets rippled and vorticity is generated as discussed in Sec. II. To calculate the downstream vorticity averages, we use Eqs. (67)–(72) for the asymptotic vorticity field amplitudes. In two dimensions, we have

$$\langle \tilde{\omega}_z^2 \rangle = \sigma_k^2 \times W_{2D}. \tag{122}$$

For the 3D average, we normalize the downstream vorticity with respect to kc_2, which adds an additional factor $\sin^2\theta$ inside the integrals. In addition, we note that there is no vorticity perpendicular to the shock surface, as there is none upstream. Hence, the vorticity vector downstream will be parallel to the shock surface:

$$\left\langle \frac{\delta\omega_\perp^2}{(kc_2)^2} \right\rangle = \sigma_k^2 \times W_{3D}, \tag{123}$$

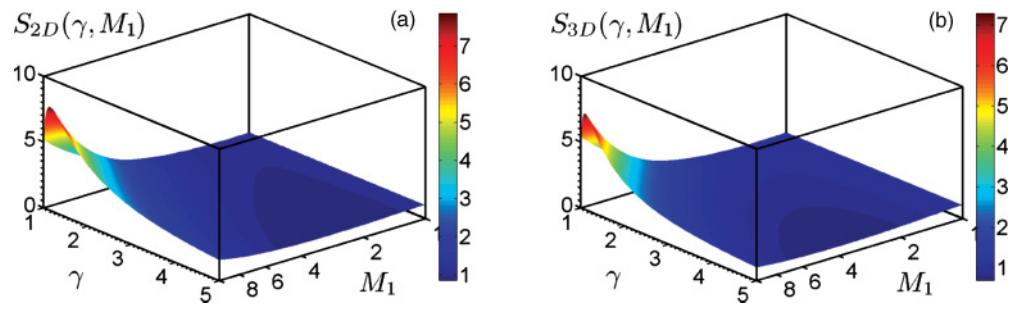

FIG. 14. (Color online) S_{2D} and S_{3D} as a function of the shock strength M_1 and γ.

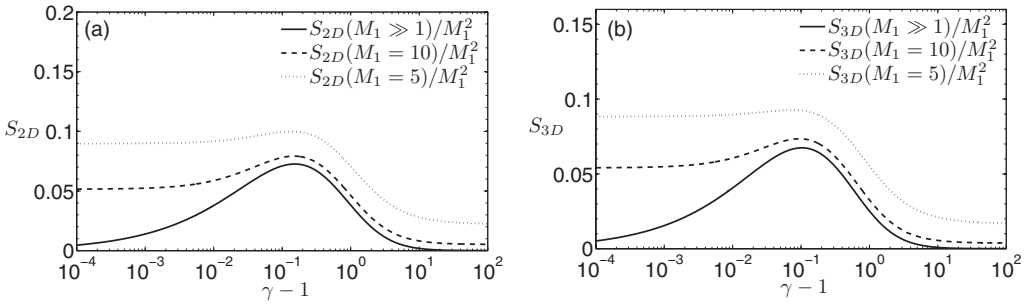

FIG. 15. S_{2D} and S_{3D} in the strong shock limit, and also for some finite values of the Mach number as a function of γ.

where the functions W_{2D} and W_{3D} are given by the integrals

$$W_{2D} = \frac{2}{\pi}\int_0^{\theta_1} \Omega_2^2(e_s-1)^2\sin^2\theta\, d\theta + \frac{2}{\pi}\int_{\theta_1}^{\theta_2} \Omega_2^2\big[e_{l1}^2 + (e_{l2}-1)^2\big]\sin^2\theta\, d\theta + \frac{2}{\pi}\int_{\theta_2}^{\pi} \Omega_2^2(e_s-1)^2\sin^2\theta d\theta,$$

$$W_{3D} = \int_0^{\theta_1} \Omega_2^2(e_s-1)^2\sin^3\theta\, d\theta + \int_{\theta_1}^{\theta_2} \Omega_2^2\big[e_{l1}^2+(e_{l2}-1)^2\big] \times \sin^3\theta\, d\theta + \int_{\theta_2}^{\pi} \Omega_2^2(e_s-1)^2\sin^3\theta\, d\theta. \quad (124)$$

In Figs. 17(a) and 17(b), we show the different contributions of the averaged vorticity for a shock into air as a function of the shock strength. In Fig. 18(a), we show the behavior of the 2D downstream squared vorticity as a function of γ and M_1. The same is done in Fig. 18(b) for the 3D case. We obtain the following strong shock asymptotic expressions for the long- and short-wavelength branch in Eqs. (B11) and (B12). The explicit formulas also agree with those shown in Eqs. (160)–(163) in Ref. [19] for the 3D shock/entropy interaction. The total vorticity generation in this limit is given in Eq. (B13), which can be simplified in the highly compressible and highly incompressible limits as

$$W_{3D}(\gamma, M_1 \gg 1) \cong \begin{cases} \frac{8}{3(\gamma-1)^2} + O\big[\frac{1}{(\gamma-1)^{3/2}}\big], & \gamma - 1 \ll 1, \\ \frac{4}{3\gamma^2} + O\big(\frac{1}{\gamma^3}\big), & \gamma \gg 1. \end{cases} \quad (125)$$

The strong shock-limiting curves in two and three dimensions are shown in Fig. 19, where they are also compared with the curves corresponding to other finite values of the shock strength ($M_1 = 5, 10$). We observe that both W_{2D} and W_{3D} diverge for highly compressible gases in the strong shock limit. On the other hand, for highly compressible gases, the long- and short-wavelength branches have the asymptotic expansions shown in Eqs. (B14) and (B15), and the sum of both contributions is given in Eq. (B16). This formula can be reduced to much more simplified expressions for very weak and very strong shocks:

$$W_{3D}(\gamma - 1 \ll 1, M_1) \cong \begin{cases} (M_1-1)^6\big[\frac{14848\sqrt{2}-4134}{15} - 64\ln(M_1-1)\big] + O[(M_1-1)^7], & M_1 - 1 \ll 1, \\ \frac{4}{5}M_1^4 + 2M_1^3\ln M_1 + M_1^3\big(2\ln 2 - \frac{103}{15}\big) + \frac{16}{5}M_1^2 + O(M_1), & M_1 \gg 1. \end{cases} \quad (126)$$

In Fig. 20, we compare Eq. (B16), the highly compressible gases limit, with other values of γ.

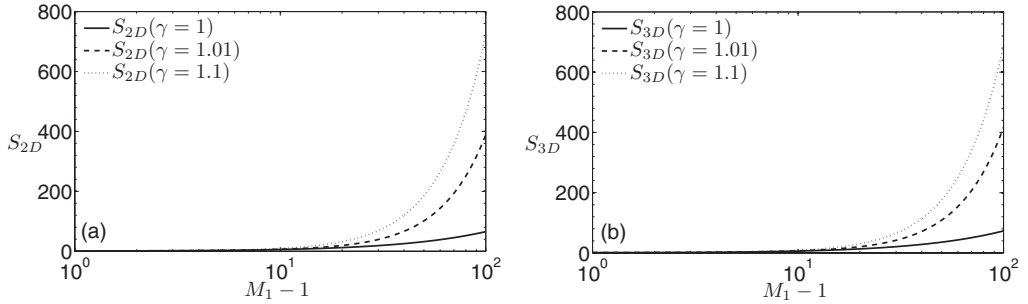

FIG. 16. S_{2D} and S_{3D} in the high compressibility limit ($\gamma = 1$), and also for some low values of γ as a function of the shock strength M_1.

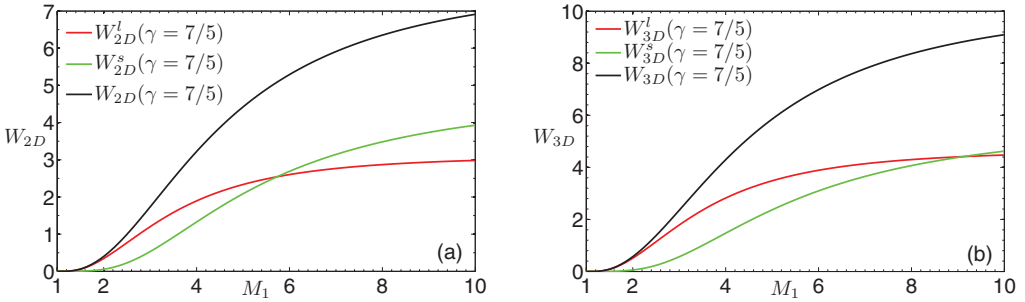

FIG. 17. (Color online) 2D and 3D vorticity generation contributions as a function of the shock strength M_1 and for $\gamma = 7/5$.

D. Density amplification

From Sec. II, we know that the density field behind the shock can be decomposed into the entropic and the acoustic component. We calculate now the amplification of the averaged density perturbations squared either in 2D or 3D. We define the dimensionless density amplification factor as

$$\frac{\langle \delta\rho_2^2 \rangle}{\langle \delta\rho_1^2 \rangle} = R^2 \frac{\langle \tilde{\rho}_2^2 \rangle}{\langle \tilde{\rho}_1^2 \rangle} = R^2 G. \tag{127}$$

The entropic part of the function G is split into the long- and short-wavelength branches as

$$G^l_{2D} = \int_{-1}^{1} \left| Q^l_{en} \right|^2 J_{2D}(\zeta_{ac}) d\zeta_{ac},$$
$$G^l_{3D} = \int_{-1}^{1} \left| Q^l_{en} \right|^2 J_{3D}(\zeta_{ac}) d\zeta_{ac}, \tag{128}$$

$$G^s_{2D} = \int_{-\infty}^{-1} \left| Q^s_{en} \right|^2 J_{2D}(\zeta_{ac}) d\zeta_{ac} + \int_{1}^{\infty} \left| Q^s_{en} \right|^2 J_{2D}(\zeta_{ac}) d\zeta_{ac},$$
$$G^s_{3D} = \int_{-\infty}^{-1} \left| Q^s_{en} \right|^2 J_{3D}(\zeta_{ac}) d\zeta_{ac} + \int_{1}^{\infty} \left| Q^s_{en} \right|^2 J_{3D}(\zeta_{ac}) d\zeta_{ac}, \tag{129}$$

and the acoustic contribution is

$$G^{ac}_{2D} = K^{ac}_{2D} = \int_{-\infty}^{-1} e_s^2 \, J_{2D}(\zeta_{ac}) d\zeta_{ac} + \int_{1}^{\infty} e_s^2 \, J_{2D}(\zeta_{ac}) d\zeta_{ac},$$
$$G^{ac}_{3D} = K^{ac}_{3D} = \int_{-\infty}^{-1} e_s^2 \, J_{3D}(\zeta_{ac}) d\zeta_{ac} + \int_{1}^{\infty} e_s^2 \, J_{3D}(\zeta_{ac}) d\zeta_{ac}. \tag{130}$$

In Figs. 21(a) and 21(b), we show the different contributions to the averaged density amplification ($G^l_{2D/3D}$, $G^s_{2D/3D}$, $G^{ac}_{2D/3D}$, and $G_{2D/3D} = G^l_{2D/3D} + G^s_{2D/3D} + G^{ac}_{2D/3D}$) as functions of the shock strength for a shock moving into air. We notice that G_{2D} tends to 0.477 236 when $M_1 \gg 1$, and the 3D value is 0.451 896. In Fig. 22(a), we show the behavior of G_{2D} as a function of γ and M_1. The same is done in Fig. 22(b) for the 3D case. In Figs. 21 and 22, we observe how the acoustic contribution is dominant for weak shocks either in two or three dimensions. From Fig. 21, we see that the total density field reaches a constant value for very strong shocks and becomes a function of γ. As in the previous subsections, we discuss here the asymptotic behavior of the density amplification factor in the strong shock limit. In order to do so, we refer to Eqs. (148)–(152) in Ref. [19], because, as was explained before, the preshock acoustic velocity and pressure become negligible in that limit, and therefore the density upstream perturbations dominate the shock dynamics. For the entropic contribution, we obtain the expressions shown in Appendix B in Eqs. (B17) and (B18). The acoustic contributions agree with the acoustic part of the turbulent kinetic energy Eq. (B3). The total density amplification Eq. (B18) is the sum of the entropic and acoustic parts, and it is simplified in the limits $\gamma - 1 \ll 1$ and $\gamma \gg 1$ as

$$G_{3D}(\gamma, M_1 \gg 1) \cong \begin{cases} 1 - \frac{5}{2}\sqrt{2(\gamma-1)} + O(\gamma - 1), & \gamma - 1 \ll 1, \\ 1 - \frac{2+\sqrt{2}}{3\gamma} + O\left(\frac{1}{\gamma^2}\right), & \gamma \gg 1. \end{cases} \tag{131}$$

In Fig. 23, we show the strong shock limit formula (B19) together with the values corresponding to $M_1 = 5, 10$. We observe that for higher values of adiabatic index γ, the curves tend to converge to $G_{2D/3D}(\gamma \gg 1, M_1 \gg 1) \to 1$, in agreement with Eq. (131).

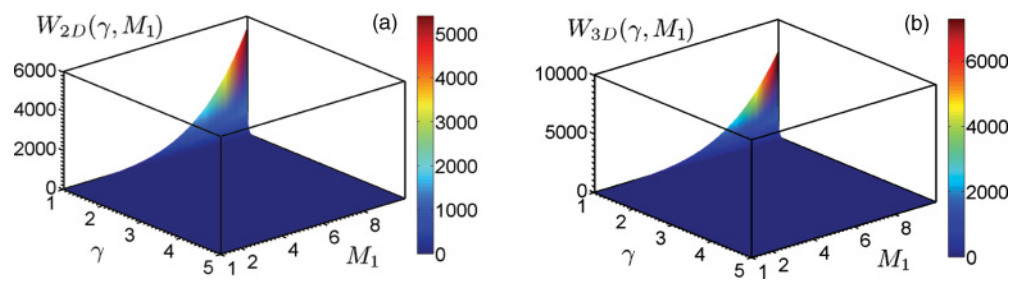

FIG. 18. (Color online) W_{2D} and W_{3D} as a function of the shock strength M_1 and γ.

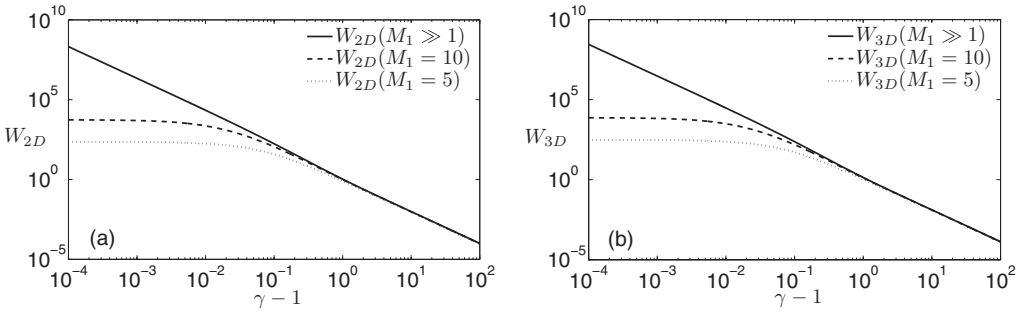

FIG. 19. W_{2D} and W_{3D} in the strong shock limit, and also for some finite values of the Mach number as a function of γ.

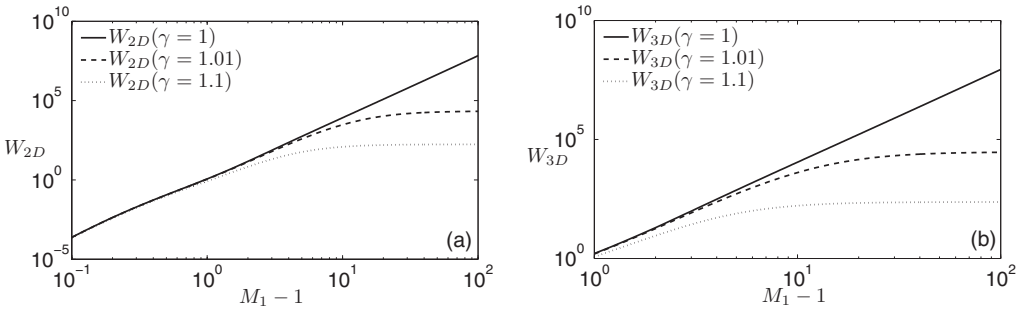

FIG. 20. W_{2D} and W_{3D} in the high compressibility limit ($\gamma = 1$), and also for some low values of γ as a function of the shock strength M_1.

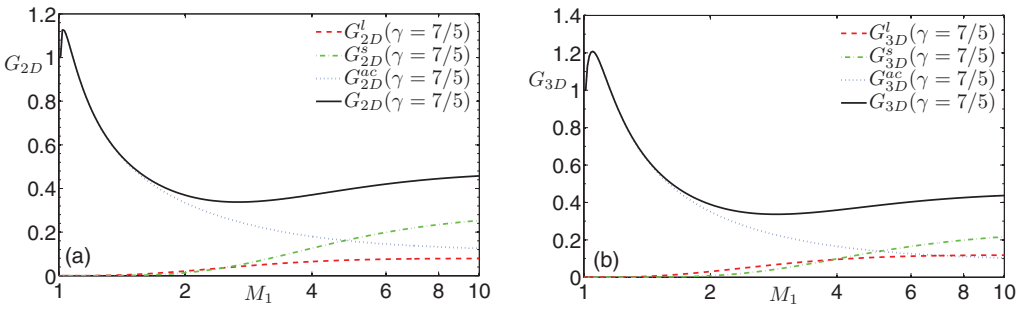

FIG. 21. (Color online) 2D and 3D density contributions as a function of the shock strength M_1 and for $\gamma = 7/5$.

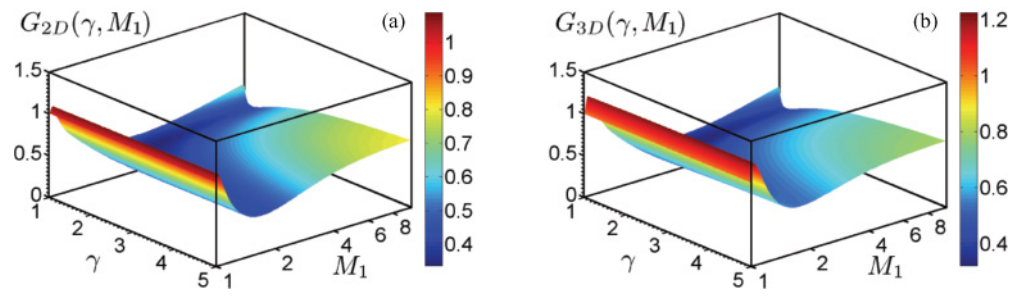

FIG. 22. (Color online) G_{2D} and G_{3D} as a function of the shock strength M_1 and γ.

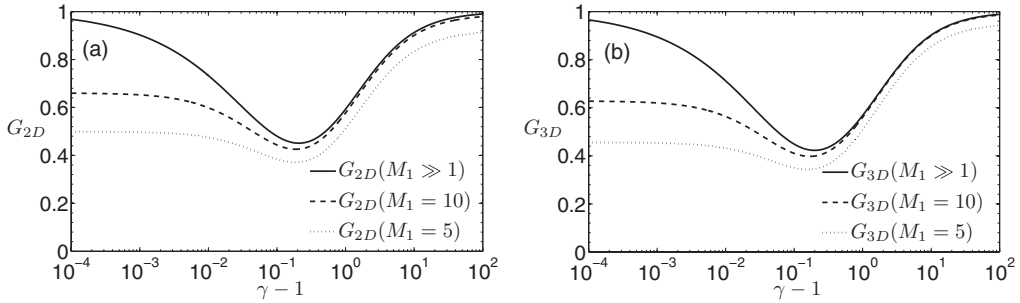

FIG. 23. G_{2D} and G_{3D} in the strong shock limit, and also for some finite values of the Mach number as a function of γ.

The highly compressible limit ($\gamma \to 1$) for the entropic part is given in Appendix B [Eqs. (B20) and (B21)], and the acoustic contribution agrees exactly with Eq. (B7) in this limit. We see that in the limit $\gamma \to 1$, the dominant term is the acoustic contribution. If we go to Eq. (16), we observe that for $\gamma \to 1$, it is $\tilde{p}_1 \sim \tilde{\rho}_1$, and hence $\tilde{p}_2 \sim \tilde{\rho}_2$, which means that the post-shock density perturbations are essentially acoustic. Because of this, $G^{\rm ac}_{\rm 2D/3D}$ is dominant over $G^{l}_{\rm 2D/3D}$ and $G^{s}_{\rm 2D/3D}$ in the highly compressible limit (see Fig. 24). If we compare this case with that studied in Ref. [19], where the shock traveled through a nonuniform entropy field, the limit $\gamma \to 1$ implied no change in the entropic perturbations, and therefore the entropic part of G approached unity in this limit. As before, the total amplification factor can be reduced to simpler expressions for very strong and very weak shocks:

$$G_{3D}(\gamma - 1 \ll 1, M_1) \cong \begin{cases} 1 + \left[\frac{98\sqrt{2}-191}{15} - 4\ln(M_1 - 1)\right](M_1 - 1) + O[(M_1 - 1)^2], & M_1 - 1 \ll 1, \\ 1 - \frac{5}{M_1} + \frac{40}{3M_1^2} + O\left(\frac{1}{M_1^3}\right), & M_1 \gg 1. \end{cases} \tag{132}$$

The weak shock limit expression for arbitrary values of γ agrees with Eq. (114). We see that there is no dependence on γ at the leading order for very weak shocks, in agreement with Fig. 22.

E. Anisotropy

In Refs. [17,19], the interaction of a shock with an upstream isotropic vorticity and an entropy field, respectively, was studied, and it was shown there that the flow behind the shock was generally anisotropic in velocity. We define here the same anisotropy parameter as in those works for the 3D perturbations:

$$\beta_v = \frac{\langle \tilde{v}_\perp^2 \rangle - 2\langle \tilde{v}_{||}^2 \rangle}{\langle \tilde{v}_\perp^2 \rangle + 2\langle \tilde{v}_{||}^2 \rangle} = 1 - 4\frac{\langle \tilde{v}_x^2 \rangle}{\langle \tilde{v}^2 \rangle + \langle \tilde{v}_x^2 \rangle}. \tag{133}$$

In the preceding equation, $\tilde{v}_\perp$ refers to the velocity component parallel to the shock and $\tilde{v}_{||}$ refers, actually, to $\tilde{v}_x$. According to Eq. (133), $\beta_v = +1$ would essentially mean that $\langle \tilde{v}_x^2 \rangle \simeq 0$, which would imply post-shock velocity perturbations parallel to the shock surface. On the other hand, $\beta_v = -1$ means that $\langle \tilde{v}_x^2 \rangle \simeq \langle \tilde{v}^2 \rangle$, and hence the velocity perturbations are perpendicularly oriented to the shock surface. In Fig. 25(a), we plot the previous parameter as a function of γ and M_1. We see that the anisotropy parameter varies between -1 and $+1$. The behavior of the anisotropy parameter in the case studied here is essentially different from the one shown in Refs. [17,19]. For very strong shocks and highly compressible gases, the anisotropy tends to 1 (totally lateral). On the other hand, a total longitudinal anisotropy ($\beta_v = -1$) is never reached for any value γ and M_1. Between these two values, we observe that velocity isotropy conditions can be found on the curve $\beta_v = 0$ as shown in Fig. 25(b).

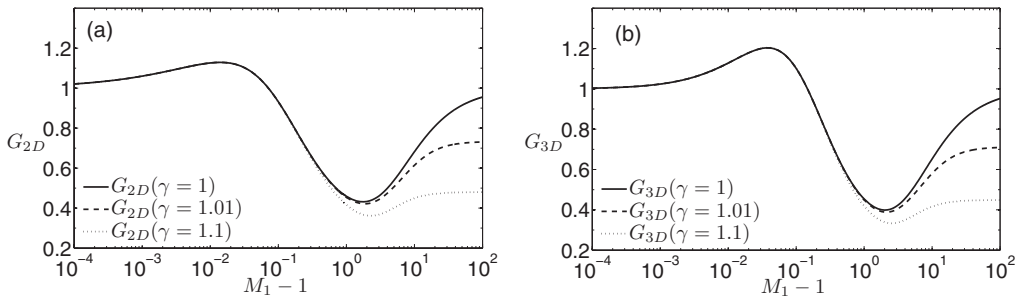

FIG. 24. G_{2D} and G_{3D} in the high compressibility limit ($\gamma = 1$), and also for some low values of γ as a function of the shock strength M_1.

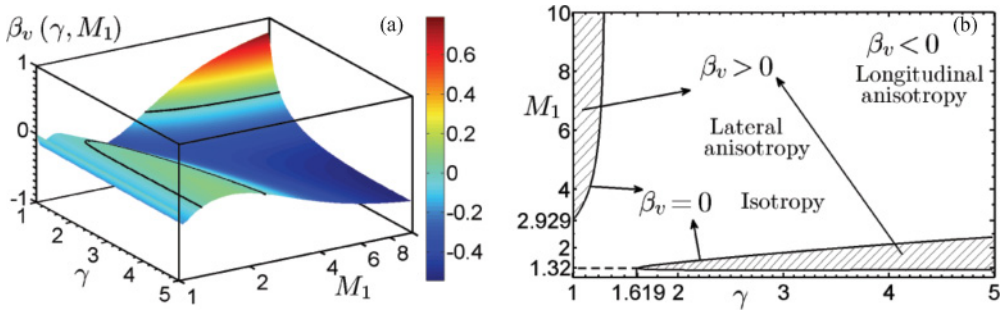

FIG. 25. (Color online) (a) β_v as a function of the shock strength M_1 and γ. (b) Level curve for $\beta_v = 0$ where the longitudinal and transverse anisotropy zones are defined.

IV. SUMMARY

We have presented an analytical theory that describes the linear interaction of an isolated planar shock wave with a field of isotropic sound waves. The interaction of the shock with a single mode is solved exactly. The wave equation downstream is solved and the generation of pressure, velocity, and density perturbations is described in detail, including the transient phase before the achievement of asymptotic conditions far downstream. The vorticity generation is described together with the corresponding rotational velocity field. The RM growth that ensues at the weak discontinuity is also studied, showing that the growth resembles the classical RM growth that occurs at a contact surface for the case of a reflected rarefaction. The emission of sound downstream is characterized as a function of the adiabatic index and the shock strength and compared to the emission of sound in the other two canonical problems, namely the "preshock vorticity" and "preshock entropy" problems. The existence of two critical angles is discussed and it is shown that the transition to the asymptotic regime downstream takes a longer time as the critical angles are approached. In order to deal with the interaction of the shock front with a full spectrum of sound waves, the usual angle averaging is performed, using the perturbation amplitudes from the single-mode theory. In this way, the averages of the turbulent kinetic energy, the acoustic flux radiated downstream, and the vorticity and density squared are studied in detail as functions of the adiabatic index γ and the shock strength M_1 for 2D and 3D isotropic spectra. Exact asymptotic expansions of these quantities in the important physical limits of very strong shocks, very weak shocks, and highly compressible fluids have been written in terms of elementary functions. The anisotropy of the downstream perturbations has also been characterized as a function of γ and M_1, and it was found that the downstream perturbations are mostly longitudinally anisotropic, except for some regions where there is the possibility of transverse anisotropy. The curves for velocity isotropy conditions have also been shown. This work closes a series of related problems, such as those of a shock interacting with the only three perturbation modes that can be excited in a normal fluid: vorticity, entropy, and sound waves. There is the possibility of addressing additional problems with more realistic boundary conditions downstream, such as the existence of a piston that drives the shock and reflects back to its surface a part of the sound waves radiated downstream. The possibility of reshocking the turbulent flow generated by a first shock wave is also another interesting problem amenable to an analytical solution with the tools presented here; this is left for future works.

ACKNOWLEDGMENTS

This work was supported by the Ministry of Science, MEC (ENE2009-09276, AP2007-02745) and Junta de CLM (PEI11-0056-1890), Spain (C.H. and J.G.W.) and by the US DOE/NNSA (A.L.V.). Encouragement from A. Bret and A. R. Piriz (UCLM) is gratefully acknowledged.

APPENDIX A: INTERACTION OF A PLANAR SHOCK WAVE WITH A LONGITUDINAL FIELD OF SOUND WAVES

In this Appendix, we present a detailed discussion of a shock interacting with a single-mode perturbation with $k_y = 0$. We analyze this particular case studying the Riemann invariants upstream and downstream, and comparing the results with those shown in Sec. II in the limit $|\zeta_{\rm ac}| \to \infty$. Following the arguments given in Ref. [26] on p. 20, the Riemann invariants $J_\pm$ for linear perturbations are given by

$$J_\pm = \Delta u \pm \frac{\Delta p}{\rho_0 c_0}, \tag{A1}$$

where Δu and Δp represent the longitudinal velocity and pressure perturbations in the fluid. The values of ρ_0 and c_0 correspond to the background values of density and speed of sound, respectively. Along the two families of characteristics $C_\pm : \frac{dx}{dt} = u \pm c$, the values of $J_\pm$ remain constant, and, therefore, the velocity Δu and pressure Δp acoustic perturbations are related as

$$\begin{aligned} \Delta u + \tfrac{\Delta p}{\rho_0 c_0} &= 2 f_1[x - (u_0 + c_0)t], \\ \Delta u - \tfrac{\Delta p}{\rho_0 c_0} &= -2 f_2[x + (u_0 - c_0)t]. \end{aligned} \tag{A2}$$

The functions f_1 and f_2 refer to the isentropic perturbations traveling to the right and to the left, respectively. We study at first the upstream field of longitudinal waves. We rewrite Eq. (A2) according to the notation used here, in the laboratory frame ($u_0 = 0$), and we get

$$\begin{aligned} \tilde{v}_{x1} + \tilde{p}_1 &= 2\tilde{f}_1(x' - c_1 t), \\ \tilde{v}_{x1} - \tilde{p}_1 &= -2\tilde{f}_2(x' + c_1 t). \end{aligned} \tag{A3}$$

For waves traveling to the right, it is $\tilde{f}_2 = 0$ and hence $\tilde{v}_{x1} = \tilde{p}_1$, which agrees with Eq. (5) of Sec. II by making $\theta = 0$. On the other hand, for acoustic waves traveling to the left, we make $\tilde{f}_1 = 0$, which gives $\tilde{v}_{x1} = -\tilde{p}_1$, which agrees with Eq. (5) by making $\theta = \pi$.

The isentropic perturbations (A2) in the compressed fluid reference frame are recast as

$$\begin{aligned} \tilde{v}_{x2} + \tilde{p}_2 &= 2\tilde{f}_1'(x - c_2 t), \\ \tilde{v}_{x2} - \tilde{p}_2 &= -2\tilde{f}_2'(x + c_2 t), \end{aligned} \tag{A4}$$

where the functions $\tilde{f}_1'$ and $\tilde{f}_2'$ refer to the isentropic perturbations downstream traveling to the right and to the left, respectively. The amplitude of the acoustic perturbations is determined by the boundary/initial conditions. In the problem considered here, where the shock travel is isolated, the function $\tilde{f}_1' = 0$ for any case. The amplitude of $\tilde{f}_2'$ is given by linearized Rankine-Hugoniot equations at the shock wave. We find two possible situations depending on whether $\theta = 0$ or $\theta = \pi$.

1. Right-traveling acoustic waves

When the upstream sonic waves are traveling to the right ($\theta = 0$), the velocity and the pressure perturbations are related as $\tilde{v}_{x1} = \tilde{p}_1$. With the aid of Eq. (14) in Sec. II and taking into account that $\tilde{f}_1' = 0$, and hence $\tilde{v}_{x2} = -\tilde{p}_2$, we arrive at

$$\tilde{v}_{x2} = -\frac{\left(M_1^2+1\right)M_2^2 R + 1 - M_1 M_2^2 (M_1 + 2R)}{2M_1^2 M_2 + M_1^2 + 1}\tilde{p}_1. \tag{A5}$$

It is easy to see that Eq. (A5) agrees exactly with $Q_{\rm ac}$ in Eq. (62) in the limit of $k_y = 0$, or equivalently by taking $\zeta_{\rm ac} \to +\infty$. The relationship $\tilde{v}_{x2} = -\tilde{p}_2$ can also be obtained by taking $\zeta_{\rm ac} \to +\infty$ in Eqs. (41) and (62). As there is no transverse flux, the rotational contribution to the velocity field is zero, and so the rotational contribution to the velocity field is zero in that limit, $Q_{\rm rot}(\zeta_{\rm ac} \to +\infty) = 0$.

We also show the density perturbations downstream. As discussed before, they can be split into the acoustic and entropic perturbations. The sonic fluctuations are directly given by $\tilde{p}_2 = \tilde{\rho}_2^{\rm ac}$, and the entropic ones are obtained by Eq. (16) after subtracting the acoustic part. Taking into account the above Eq. (A5), we arrive at

$$\tilde{\rho}_2^{\rm en} = -\frac{1 - M_1^2 M_2^2}{M_1^2 M_2^2} \times \left[\frac{\left(M_1^2+1\right)M_2^2 R + 1 - M_1 M_2^2 (M_1 + 2R)}{2M_1^2 M_2 + M_1^2 + 1} + 1\right]\tilde{p}_1. \tag{A6}$$

We notice that Eq. (A6) is exactly the same as $Q_{\rm en}$ in Eq. (96) in the limit $\zeta_{\rm ac} \to +\infty$.

2. Left-traveling acoustic waves

If the acoustic waves ahead of the shock are traveling to the left impinging on the shock front, $\tilde{f}_1 = 0$ and hence $\tilde{v}_{x1} = -\tilde{p}_1$. It modifies Eq. (14) with respect to that obtained in Eq. (A6). The new amplitude for the velocity field downstream is

$$\tilde{v}_{x2} = -\frac{\left(M_1^2+1\right)M_2^2 R + 1 - M_1 M_2^2 (M_1 - 2R)}{2M_1^2 M_2 + M_1^2 + 1}\tilde{p}_1. \tag{A7}$$

As before, Eq. (A7) agrees with $Q_{\rm ac}$ in Eq. (62) by taking $\zeta_{\rm ac} \to -\infty$. The pressure is also given by $\tilde{v}_{x2} = -\tilde{p}_2$. We can observe that the absolute value of $\tilde{v}_{x2}$ is greater in Eq. (A7) than in Eq. (A5). This effect can be seen in Fig. 4 in Sec. II, where the acoustic power emitted by the shock is larger for the outer curves than for the inner curves. The outer curves are due to the left-traveling upstream wave, while the inner ones are due to the right-traveling sonic modes.

The entropic density perturbations are directly obtained with the aid of Eqs. (16) and (A7). They are

$$\tilde{\rho}_2^{\rm en} = -\frac{1 - M_1^2 M_2^2}{M_1^2 M_2^2} \times \left[\frac{\left(M_1^2+1\right)M_2^2 R + 1 - M_1 M_2^2 (M_1 - 2R)}{2M_1^2 M_2 + M_1^2 + 1} + 1\right]\tilde{p}_1, \tag{A8}$$

which agrees with Eq. (96) when $\zeta_{\rm ac} \to -\infty$.

APPENDIX B: 3D ASYMPTOTIC EXPRESSIONS

In this Appendix, we show the exact expressions for the strong shock limit $M_1 \gg 1$ or the high compressibility limit $\gamma - 1 \ll 1$. For the quantities of interest, they are the kinetic energy amplification, the acoustic energy flux, the vorticity generation, and the density amplification.

1. Downstream kinetic energy

The 3D kinetic energy can be decomposed into the rotational (long and short branches) contribution and the acoustic contribution. In the strong shock limit $M_1 \gg 1$, the long-wavelength part is

$$K_{\rm 3D}^{l}(\gamma, M_1 \gg 1) \cong \frac{\sqrt{\gamma - 1}}{\sqrt{2\gamma}} + \frac{(\gamma+1)(2-\gamma)}{2\sqrt{2\gamma(\gamma-1)}} \ln\left(\frac{\gamma+1}{\gamma-1}\right), \tag{B1}$$

whereas the short-wavelength branch gives

$$K_{\rm 3D}^{s}(\gamma, M_1 \gg 1) \cong -\frac{3\gamma^2 - \gamma - 1}{2\gamma - 1} + \frac{6\gamma^3 - 5\gamma^2 - 4\gamma + 1}{(2\gamma-1)\sqrt{2\gamma(\gamma-1)}} + \frac{(\gamma+1)^2}{(2\gamma-1)^2\sqrt{\gamma}} \tan^{-1}\left(\frac{1}{\sqrt{\gamma}}\right) + \frac{\gamma(\gamma+1)(2\gamma-3)(3\gamma^2-4\gamma+2)}{(2\gamma-1)^2\sqrt{2\gamma(\gamma-1)}} \ln\left[\frac{\gamma(\gamma-1)+\sqrt{2\gamma(\gamma-1)}}{\gamma(\gamma+1)}\right]. \tag{B2}$$

The acoustic contribution for very strong shocks scales as follows:

$$K_{3D}^{ac}(\gamma, M_1 \gg 1) \cong -\frac{3\gamma^4 - 6\gamma^3 - \gamma^2 + 4\gamma - 1}{\gamma(2-\gamma)} + \frac{(2\gamma-1)(3\gamma^2 - 3\gamma - 5)\sqrt{\gamma-1}}{\sqrt{2\gamma}(2-\gamma)} - \frac{3}{2}(\gamma^2-1)\sqrt{2\gamma(\gamma-1)}\ln\left[\frac{\gamma(\gamma-1)+\sqrt{2\gamma(\gamma-1)}}{\gamma(\gamma+1)}\right]. \tag{B3}$$

The total kinetic energy in that limit is thus given by the sum of the previous expressions:

$$K_{3D}(\gamma, M_1 \gg 1) \cong -\frac{(\gamma-1)(6\gamma^4 - 12\gamma^3 - \gamma^2 + 7\gamma - 1)}{\gamma(2-\gamma)(2\gamma-1)} + \frac{12\gamma^5 - 42\gamma^4 + 34\gamma^3 + 23\gamma^2 - 38\gamma + 9}{(2-\gamma)(2\gamma-1)\sqrt{2\gamma(\gamma-1)}} + \frac{(\gamma+1)^2}{(2\gamma-1)^2\sqrt{\gamma}}\tan^{-1}\left(\frac{1}{\sqrt{\gamma}}\right) + \frac{(\gamma+1)(2-\gamma)}{2\sqrt{2\gamma(\gamma-1)}}\ln\left(\frac{\gamma+1}{\gamma-1}\right) - \frac{(\gamma+1)(12\gamma^4 - 42\gamma^3 + 56\gamma^2 - 34\gamma + 9)}{2(2\gamma-1)^2(\gamma-1)} \times \sqrt{2\gamma(\gamma-1)}\ln\left[\frac{\gamma(\gamma-1)+\sqrt{2\gamma(\gamma-1)}}{\gamma(\gamma+1)}\right]. \tag{B4}$$

For very compressible fluids, in the limit $\gamma - 1 \ll 1$, the kinetic energy only depends on the incident shock strength. We get in that limit, for the long- and short-wavelength contributions,

$$K_{3D}^{l}(\gamma - 1 \ll 1, M_1) \cong \frac{\left(M_1^2-1\right)^3\left(6M_1^{14} - 4M_1^{12} - 21M_1^{10} + 18M_1^8 + 9M_1^6 - 21M_1^4 + 18M_1^2 - 5\right)}{3M_1^4\left(M_1^2+1\right)^{5/2}\left(M_1^4 + M_1^2 - 1\right)^3} + \frac{\left(M_1^2-1\right)^3\left(M_1^8 + 6M_1^4 + 1\right)}{M_1^5\left(M_1^2+1\right)^4}\ln\left(M_1 + \sqrt{M_1^2+1}\right) + \frac{4\left(M_1^2-1\right)^3\left(M_1^4+1\right)}{M_1^3\left(M_1^2+1\right)^4}\ln\left(\frac{\sqrt{M_1^4+M_1^2-1}}{M_1\sqrt{M_1^2+1}+1}\right), \tag{B5}$$

$$\begin{aligned} K_{3D}^{s}(\gamma - 1 \ll 1, M_1) \cong & -\frac{(M_1-1)}{3M_1^8\left(M_1^2+1\right)^5\left(M_1^4+M_1^2-1\right)^2}\left(M_1^{25} - 4M_1^{23} - 32M_1^{22} + 61M_1^{21}\right. \\ & \left. - 318M_1^{20} + 250M_1^{19} - 418M_1^{18} + 237M_1^{17} + 75M_1^{16} + 87M_1^{15} + 96M_1^{14} - 34M_1^{13} + 854M_1^{12}\right. \\ & \left. - 318M_1^{11} + 399M_1^{10} - 68M_1^9 - 1241M_1^8 + 163M_1^7 + 444M_1^6 - 21M_1^5 - 44M_1^4 - 2M_1^3 + 31M_1^2 - 6\right) \\ & - \frac{\left(M_1^2-1\right)}{3M_1^8\left(M_1^2+1\right)^{9/2}\left(M_1^4+M_1^2-1\right)^3}\left(5M_1^{28} + 18M_1^{26} + 148M_1^{24} + 290M_1^{22} - 193M_1^{20} - 495M_1^{18}\right. \\ & \left. - 496M_1^{16} - 758M_1^{14} + 1429M_1^{12} + 954M_1^{10} - 1512M_1^8 + 458M_1^6 - 71M_1^4 + 37M_1^2 - 6\right) \\ & + \frac{2(M_1-1)^2M_1^4(M_1+1)^2\left(M_1^6 - M_1^4 - M_1^2 - 1\right)}{\left(M_1^2+1\right)^6\sqrt{M_1^4 - M_1^2 - 1}}\left[\tan^{-1}\left(\sqrt{M_1^4 - M_1^2 - 1}\right)\right. \\ & \left. + \tan^{-1}\left(\frac{\sqrt{M_1^4 - M_1^2 - 1}}{M_1}\right) - \tan^{-1}\left(\frac{\sqrt{M_1^4 - M_1^2 - 1}}{\sqrt{M_1^2+1}}\right)\right] \\ & - \frac{\left(M_1^{18} - 8M_1^{16} + 12M_1^{14} + 14M_1^{12} - 98M_1^{10} + 154M_1^8 - 112M_1^6 + 34M_1^4 + M_1^2 - 2\right)\left(M_1^2-1\right)^2}{2M_1^9\left(M_1^2+1\right)^6} \\ & \times \ln\left(\frac{M_1+1}{M_1-1}\right) + \frac{1}{2M_1^9\left(M_1^2+1\right)^6}\left(M_1^{22} - 2M_1^{20} + 41M_1^{18} + 38M_1^{16} - 34M_1^{14} + 116M_1^{12}\right. \\ & \left. - 374M_1^{10} + 140M_1^8 - 87M_1^6 + 30M_1^4 + 5M_1^2 - 2\right)\ln\left(\frac{M_1^2+1}{M_1^2-1}\right) + \frac{1}{M_1^9\left(M_1^2+1\right)^6}\left(M_1^{22} - 2M_1^{20}\right. \\ & \left. + 41M_1^{18} + 38M_1^{16} - 34M_1^{14} + 116M_1^{12} - 374M_1^{10} + 140M_1^8 - 87M_1^6 + 30M_1^4 + 5M_1^2 - 2\right) \\ & \times \ln\left(M_1 + \sqrt{M_1^2+1}\right) + \frac{4\left(2M_1^{14} + 3M_1^{12} + 14M_1^{10} + 20M_1^8 - 62M_1^6 + 36M_1^4 - 68M_1^2 + 23\right)}{M_1^3\left(M_1^2+1\right)^6} \end{aligned}$$

$$\times \ln\left(\frac{\sqrt{M_1^4+M_1^2-1}}{M_1\sqrt{M_1^2+1}+1}\right)+\frac{1}{M_1^4\left(M_1^2+1\right)^6\left(M_1^4+M_1^2-1\right)^{5/2}}\left(2M_1^{26}+17M_1^{24}+44M_1^{22}\right.$$
$$+136M_1^{20}+143M_1^{18}-466M_1^{16}-514M_1^{14}+392M_1^{12}-136M_1^{10}+219M_1^8+538M_1^6-736M_1^4$$
$$\left.+251M_1^2-18\right)\ln\left(\frac{\sqrt{M_1^4-1}}{\sqrt{M_1^4+M_1^2-1}+M_1}\right). \tag{B6}$$

We realize that the argument of $\tan^{-1}(\sqrt{M_1^4-M_1^2-1})$ becomes imaginary for Mach numbers lower than $\sqrt{1+\sqrt{5}}/\sqrt{2}\cong 1.272$. Nevertheless, the total expression remains real-valued for any $M_1\geqslant 1$. For the acoustic contribution, we have

$$K_{3D}^{ac}(\gamma-1\ll 1,M_1)\cong\frac{1}{3M_1^6(M_1+1)\left(M_1^2+1\right)\left(M_1^4-1\right)^3\left(M_1^4+M_1^2-1\right)^2}\left(3M_1^{29}-9M_1^{28}\right.$$
$$+37M_1^{27}-75M_1^{26}+190M_1^{25}-314M_1^{24}+668M_1^{23}-512M_1^{22}+893M_1^{21}+1513M_1^{20}-499M_1^{19}$$
$$+3741M_1^{18}-1717M_1^{17}+1063M_1^{16}-1169M_1^{15}-325M_1^{14}-64M_1^{13}-4320M_1^{12}+1562M_1^{11}$$
$$\left.-3154M_1^{10}+483M_1^9+5847M_1^8-735M_1^7-1727M_1^6+84M_1^5+164M_1^4+8M_1^3-124M_1^2+24\right)$$
$$+\frac{1}{3M_1^6\sqrt{M_1^2+1}\left(M_1^4-1\right)^3\left(M_1^4+M_1^2-1\right)^3}\left(3M_1^{30}+62M_1^{28}+337M_1^{26}+1806M_1^{24}\right.$$
$$+3881M_1^{22}+876M_1^{20}-3542M_1^{18}-3964M_1^{16}-4815M_1^{14}+6086M_1^{12}+6057M_1^{10}$$
$$\left.-6874M_1^8+1771M_1^6-272M_1^4+148M_1^2-24\right)-\frac{2\left(M_1^2-1\right)^3\left(2M_1^8+M_1^6-10M_1^4+9M_1^2+2\right)}{M_1^7\left(M_1^2+1\right)^5}$$
$$\times\ln\left(\frac{M_1+1}{M_1-1}\right)+\frac{2}{M_1^7\left(M_1^2+1\right)\left(M_1^4-1\right)^4}\left(3M_1^{22}+11M_1^{20}+85M_1^{18}+174M_1^{16}+50M_1^{14}\right.$$
$$\left.+286M_1^{12}-426M_1^{10}+140M_1^8-101M_1^6+31M_1^4+5M_1^2-2\right)\ln\left(\frac{M_1^2+1}{M_1^2-1}\right)$$
$$+\frac{4}{M_1^7\left(M_1^2+1\right)\left(M_1^4-1\right)^4}\left(3M_1^{22}+11M_1^{20}+85M_1^{18}+174M_1^{16}+50M_1^{14}+286M_1^{12}-426M_1^{10}\right.$$
$$\left.+140M_1^8-101M_1^6+31M_1^4+5M_1^2-2\right)\ln\left(M_1+\sqrt{M_1^2+1}\right)+\frac{4}{M_1\left(M_1^2+1\right)\left(M_1^4-1\right)^4}$$
$$\times\left(M_1^{16}+24M_1^{14}+60M_1^{12}+144M_1^{10}+286M_1^8-232M_1^6+204M_1^4-320M_1^2+89\right)$$
$$\times\ln\left(\frac{\sqrt{M_1^4+M_1^2-1}}{M_1\sqrt{M_1^2+1}+1}\right)+\frac{4}{M_1^2\left(M_1^2+1\right)\left(M_1^4-1\right)^4\left(M_1^4+M_1^2-1\right)^{5/2}}\left(7M_1^{26}+64M_1^{24}\right.$$
$$+189M_1^{22}+402M_1^{20}+515M_1^{18}-406M_1^{16}-1014M_1^{14}+208M_1^{12}-51M_1^{10}+200M_1^8+737M_1^6$$
$$\left.-834M_1^4+257M_1^2-18\right)\ln\left(\frac{\sqrt{M_1^4-1}}{\sqrt{M_1^4+M_1^2-1}+M_1}\right). \tag{B7}$$

The total kinetic energy in the highly compressible limit is

$$K_{3D}(\gamma-1\ll 1,M_1)\cong\frac{1}{3M_1^8(M_1+1)\left(M_1^2+1\right)^2\left(M_1^4-1\right)^3\left(M_1^4+M_1^2-1\right)^2}\left(2M_1^{33}-9M_1^{32}\right.$$
$$+48M_1^{31}-52M_1^{30}+144M_1^{29}-199M_1^{28}+880M_1^{27}-1488M_1^{26}+1941M_1^{25}+1034M_1^{24}+3M_1^{23}$$
$$+6726M_1^{22}-2317M_1^{21}+2530M_1^{20}-2528M_1^{19}+3897M_1^{18}-2122M_1^{17}-6623M_1^{16}+2748M_1^{15}$$
$$-11956M_1^{14}+1888M_1^{13}+12701M_1^{12}-1266M_1^{11}-4114M_1^{10}+187M_1^9+1848M_1^8$$

$$
\begin{aligned}
&- 143M_1^7 - 790M_1^6 + 21M_1^5 + 104M_1^4 + 2M_1^3 - 31M_1^2 + 6\big) \\
&+ \frac{1}{3M_1^8\left(M_1^2+1\right)^{3/2}\left(M_1^4-1\right)^3\left(M_1^4+M_1^2-1\right)^3}\big(5M_1^{36} - 5M_1^{34} + 199M_1^{32} + 166M_1^{30} \\
&+ 1501M_1^{28} + 7353M_1^{26} + 4076M_1^{24} - 3776M_1^{22} - 3805M_1^{20} - 16528M_1^{18} + 6603M_1^{16} \\
&+ 18240M_1^{14} - 14199M_1^{12} + 4823M_1^{10} - 2312M_1^8 + 826M_1^6 - 126M_1^4 + 37M_1^2 - 6\big) \\
&+ \frac{2M_1^4\left(M_1^2-1\right)^2\left(M_1^6-M_1^4-M_1^2-1\right)}{\left(M_1^2+1\right)^6\sqrt{M_1^4-M_1^2-1}}\left[\tan^{-1}\left(\sqrt{M_1^4-M_1^2-1}\right)\right. \\
&\left.+ \tan^{-1}\left(\frac{\sqrt{M_1^4-M_1^2-1}}{M_1}\right) - \tan^{-1}\left(\frac{\sqrt{M_1^4-M_1^2-1}}{\sqrt{M_1^2+1}}\right)\right] - \frac{\left(M_1^2-1\right)^2}{2M_1^9\left(M_1^2+1\right)^6} \\
&\times \left(M_1^{18} - 8M_1^{16} + 20M_1^{14} + 18M_1^{12} - 146M_1^{10} + 186M_1^8 - 64M_1^6 - 2M_1^4 - 7M_1^2 - 2\right) \\
&\times \ln\left(\frac{M_1+1}{M_1-1}\right) + \frac{1}{2M_1^9\left(M_1^2-1\right)^4\left(M_1^2+1\right)^6}\left(M_1^{30} - 6M_1^{28} + 67M_1^{26} - 86M_1^{24} + 453M_1^{22}\right. \\
&\left.+ 1350M_1^{20} - 257M_1^{18} + 3850M_1^{16} - 3949M_1^{14} + 1686M_1^{12} - 1415M_1^{10} + 366M_1^8 - 25M_1^6\right. \\
&\left.+ 10M_1^4 + 5M_1^2 - 2\right)\ln\left(\frac{M_1^2+1}{M_1^2-1}\right) + \frac{1}{M_1^9\left(M_1^2-1\right)^4\left(M_1^2+1\right)^6}\left(2M_1^{30} - 11M_1^{28} + 81M_1^{26}\right. \\
&- 116M_1^{24} + 488M_1^{22} + 1359M_1^{20} - 333M_1^{18} + 3926M_1^{16} - 3958M_1^{14} + 1651M_1^{12} - 1385M_1^{10} \\
&\left.+ 352M_1^8 - 20M_1^6 + 9M_1^4 + 5M_1^2 - 2\right)\ln\left(M_1+\sqrt{M_1^2+1}\right) + \frac{4}{M_1^3\left(M_1^2-1\right)^4\left(M_1^2+1\right)^6} \\
&\times \left(3M_1^{22} - 9M_1^{20} + 48M_1^{18} + 53M_1^{16} + 130M_1^{14} + 795M_1^{12} - 610M_1^{10} + 757M_1^8 - 817M_1^6\right. \\
&\left.+ 206M_1^4 - 66M_1^2 + 22\right)\ln\left(\frac{\sqrt{M_1^4+M_1^2-1}}{M_1\sqrt{M_1^2+1}+1}\right) + \frac{1}{M_1^4\left(M_1^2-1\right)^4\left(M_1^2+1\right)^6\left(M_1^4+M_1^2-1\right)^{5/2}} \\
&\times \left(2M_1^{34} + 9M_1^{32} + 16M_1^{30} + 338M_1^{28} + 809M_1^{26} + 1983M_1^{24} + 5376M_1^{22} - 348M_1^{20} - 8461M_1^{18}\right. \\
&\left.+ 1481M_1^{16} - 2608M_1^{14} - 42M_1^{12} + 9159M_1^{10} - 7759M_1^8 + 2752M_1^6 - 892M_1^4 + 251M_1^2 - 18\right) \\
&\times \ln\left(\frac{\sqrt{M_1^4-1}}{\sqrt{M_1^4+M_1^2-1}+M_1}\right). \qquad \text{(B8)}
\end{aligned}
$$

2. Acoustic energy flux

As was done for the kinetic energy, we show the exact limits for the acoustic energy flux given in Eq. (118). For very strong shocks we have

$$
\begin{aligned}
S_{3D}(\gamma, M_1 \gg 1) \cong &\left\{\frac{3(\gamma-1)(12\gamma^4-24\gamma^3-7\gamma^2+25\gamma-10)}{16(2\gamma-1)^2(2-\gamma)} - \frac{3(6\gamma^4-15\gamma^3+2\gamma^2+13\gamma-7)\sqrt{2\gamma(\gamma-1)}}{8(2\gamma-1)^2(2-\gamma)}\right. \\
&- \frac{3(\gamma^2-1)(6\gamma^2-9\gamma+5)}{16\sqrt{\gamma}(2\gamma-1)^3}\tan^{-1}\left(\frac{1}{\sqrt{\gamma}}\right) + \frac{3(\gamma-1)^2(\gamma+1)(6\gamma^3-3\gamma^2+1)}{8\gamma(2\gamma-1)^3}\sqrt{2\gamma(\gamma-1)} \\
&\left.\times \ln\left[\frac{\gamma(\gamma-1)+\sqrt{2\gamma(\gamma-1)}}{\gamma(\gamma+1)}\right]\right\} M_1^2 + O(M_1). \qquad \text{(B9)}
\end{aligned}
$$

For highly compressible gases ($\gamma \to 1$), the relative acoustic flux shows the scaling:

$$
\begin{aligned}
S_{3D}(\gamma - 1 \ll 1, M_1) \cong &\frac{1}{4M_1^6(M_1+1)\left(M_1^2+1\right)^5\left(M_1^4-1\right)\left(M_1^4-M_1^2-1\right)\left(M_1^4+M_1^2-1\right)^2} \\
&\times \left(3M_1^{34} - 3M_1^{33} + 31M_1^{32} - 22M_1^{31} + 127M_1^{30} - 166M_1^{29} + 188M_1^{28} - 438M_1^{27} - 449M_1^{26}\right. \\
&\left.+ 193M_1^{25} - 2307M_1^{24} + 1802M_1^{23} - 1208M_1^{22} + 1437M_1^{21} + 3683M_1^{20} - 602M_1^{19} + 4345M_1^{18}\right.
\end{aligned}
$$

$$
\begin{aligned}
&- 2230M_1^{17} + 4940M_1^{16} - 2712M_1^{15} - 2649M_1^{14} + 727M_1^{13} - 10567M_1^{12} + 2376M_1^{11} \\
&+ 3701M_1^{10} - 116M_1^9 + 2988M_1^8 - 540M_1^7 - 942M_1^6 + 30M_1^5 - 4M_1^4 + 8M_1^3 - 112M_1^2 + 24\big) \\
&+ \frac{1}{4M_1^6\left(M_1^2+1\right)^{9/2}\left(M_1^4-1\right)\left(M_1^4-M_1^2-1\right)\left(M_1^4+M_1^2-1\right)^2}\left(3M_1^{30} + 95M_1^{28} + 370M_1^{26}\right. \\
&+ 1020M_1^{24} - 115M_1^{22} - 3465M_1^{20} - 2797M_1^{18} - 2571M_1^{16} + 2696M_1^{14} + 8674M_1^{12} \\
&- 3913M_1^{10} - 2573M_1^8 + 956M_1^6 - 4M_1^4 + 112M_1^2 - 24\big) \\
&+ \frac{M_1^{20} - 6M_1^{18} + 26M_1^{16} - 68M_1^{14} + 46M_1^{12} + 48M_1^{10} + 8M_1^8 - 60M_1^6 - 31M_1^4 + 6M_1^2 - 2}{4\left(M_1^2+1\right)^6\left(M_1^4-1\right)\left(M_1^4-M_1^2-1\right)^{3/2}} \\
&\times 3M_1^2\left[\tan^{-1}\left(\sqrt{M_1^4-M_1^2-1}\right) + \tan^{-1}\left(\frac{\sqrt{M_1^4-M_1^2-1}}{M_1}\right) - \tan^{-1}\left(\frac{\sqrt{M_1^4-M_1^2-1}}{\sqrt{M_1^2+1}}\right)\right] \\
&+ \frac{2M_1^{20} - 19M_1^{18} + 42M_1^{16} - 22M_1^{14} - 69M_1^{12} + 201M_1^{10} - 220M_1^8 + 120M_1^6 - 25M_1^4 - 4M_1^2 + 2}{2\left(M_1^2-1\right)M_1^7\left(M_1^2+1\right)^7} \\
&\times 3\ln\left(\frac{M_1+1}{M_1-1}\right) - \frac{3}{2\left(M_1^2-1\right)^2M_1^7\left(M_1^2+1\right)^7}\left(7M_1^{22} + 9M_1^{20} + 118M_1^{18} + 110M_1^{16} + 118M_1^{14}\right. \\
&+ 154M_1^{12} - 292M_1^{10} + 92M_1^8 - 85M_1^6 + 21M_1^4 + 6M_1^2 - 2\big)\ln\left(\frac{M_1^2+1}{M_1^2-1}\right) \\
&+ \frac{3}{M_1^7\left(M_1^2-1\right)^2\left(M_1^2+1\right)^7}\left(7M_1^{22} + 9M_1^{20} + 118M_1^{18} + 110M_1^{16} + 118M_1^{14} + 154M_1^{12}\right. \\
&- 292M_1^{10} + 92M_1^8 - 85M_1^6 + 21M_1^4 + 6M_1^2 - 2\big)\ln\left(M_1 + \sqrt{M_1^2+1}\right) \\
&- \frac{3\left(5M_1^{16} + 30M_1^{14} + 57M_1^{12} + 174M_1^{10} + 165M_1^8 - 116M_1^6 + 129M_1^4 - 248M_1^2 + 60\right)}{M_1\left(M_1^2+1\right)^5\left(M_1^4-1\right)^2} \\
&\times \ln\left(\frac{\sqrt{M_1^4+M_1^2-1}}{M_1\sqrt{M_1^2+1}+1}\right) + \frac{3}{4M_1^2\left(M_1^2+1\right)^5\left(M_1^4-1\right)^2\left(M_1^4+M_1^2-1\right)^{5/2}}\left(M_1^{28} + 59M_1^{26}\right. \\
&+ 311M_1^{24} + 799M_1^{22} + 1667M_1^{20} + 1517M_1^{18} - 1980M_1^{16} - 2814M_1^{14} + 563M_1^{12} - 655M_1^{10} \\
&+ 1371M_1^8 + 2015M_1^6 - 2535M_1^4 + 743M_1^2 - 38\big)\ln\left(\frac{\sqrt{M_1^4-1}}{\sqrt{M_1^4+M_1^2-1}+M_1}\right). \qquad \text{(B10)}
\end{aligned}
$$

3. Vorticity downstream

The vorticity perturbations generated downstream can also be expressed in terms of γ for very strong shocks. The long-wavelength contribution is

$$
W_{3\mathrm{D}}^{l}(\gamma, M_1 \gg 1) \cong \frac{6\gamma^3 - 3\gamma^2 - 16\gamma + 1}{3(\gamma-1)\sqrt{2\gamma(\gamma-1)}} + \frac{(\gamma-2)(\gamma+1)^2(2\gamma-1)}{2(\gamma-1)\sqrt{2\gamma(\gamma-1)}}\ln\left(\frac{\gamma+1}{\gamma-1}\right). \qquad \text{(B11)}
$$

In addition, the short-wavelength branch has the asymptotic,

$$
\begin{aligned}
W_{3\mathrm{D}}^{s}(\gamma, M_1 \gg 1) \cong{}& \frac{-15\gamma^4 + 6\gamma^3 + 29\gamma^2 - 6\gamma - 6}{3(\gamma-1)^2} - \frac{30\gamma^4 + 3\gamma^3 - 59\gamma^2 - 19\gamma + 5}{3(\gamma-1)\sqrt{2\gamma(\gamma-1)}} \\
&+ \frac{\gamma(\gamma+1)^2(5\gamma^2 - 12\gamma + 6)}{2(\gamma-1)\sqrt{2\gamma(\gamma-1)}}\ln\left[\frac{\gamma(\gamma-1) + \sqrt{2\gamma(\gamma-1)}}{\gamma(\gamma+1)}\right]. \qquad \text{(B12)}
\end{aligned}
$$

The total averaged vorticity scales as

$$W_{3D}(\gamma, M_1 \gg 1) \cong \frac{-15\gamma^4+6\gamma^3+29\gamma^2-6\gamma-6}{3(\gamma-1)^2}+\frac{(\gamma+1)(30\gamma^3-21\gamma^2-41\gamma+6)}{3(\gamma-1)\sqrt{2\gamma(\gamma-1)}}+\frac{\gamma(\gamma+1)^2(5\gamma^2-12\gamma+6)}{2(\gamma-1)\sqrt{2\gamma(\gamma-1)}}$$
$$\times \ln\left[\frac{\gamma(\gamma-1)+\sqrt{2\gamma(\gamma-1)}}{\gamma(\gamma+1)}\right]-\frac{(\gamma-2)(\gamma+1)^2(2\gamma-1)}{2(\gamma-1)\sqrt{2\gamma(\gamma-1)}}\ln\left(\frac{\gamma+1}{\gamma-1}\right). \tag{B13}$$

On the other hand, the highly compressible gases limit is written in terms of the shock strength M_1. The long- and short-wavelength contributions are

$$W^l_{3D}(\gamma-1\ll 1, M_1) \cong -\frac{\left(M_1^2-1\right)^4}{15M_1^4\left(M_1^2+1\right)^{7/2}\left(M_1^4+M_1^2-1\right)^5}\left(15M_1^{26}+35M_1^{24}+148M_1^{22}+463M_1^{20}\right.$$
$$\left.+\ 140M_1^{18}-685M_1^{16}+90M_1^{14}+490M_1^{12}-670M_1^{10}+95M_1^8+340M_1^6-365M_1^4+177M_1^2-33\right)$$
$$+\frac{2\left(M_1^2-1\right)^3\left(M_1^4+3\right)\left(3M_1^4+1\right)}{M_1^3\left(M_1^2+1\right)^5}\ln\left(\frac{\sqrt{M_1^4+M_1^2-1}}{M_1\sqrt{M_1^2+1}+1}\right)+\frac{\left(M_1^2-1\right)^3\left(M_1^4+1\right)}{M_1^5\left(M_1^2+1\right)^5}$$
$$\times\left(M_1^4-2M_1^3+2M_1^2+2M_1+1\right)\left(M_1^4+2M_1^3+2M_1^2-2M_1+1\right)\ln\left(\frac{\sqrt{M_1^4-1}}{\sqrt{M_1^4+M_1^2-1}+M_1}\right), \tag{B14}$$

$$W^s_{3D}(\gamma-1\ll 1, M_1)\frac{(M_1-1)^2}{60M_1^8\left(M_1^2+1\right)^6\left(M_1^4+M_1^2-1\right)^4}\left(48M_1^{38}-96M_1^{37}+492M_1^{36}-912M_1^{35}\right.$$
$$+\ 3268M_1^{34}-2065M_1^{33}+9566M_1^{32}+15942M_1^{31}+20406M_1^{30}+85161M_1^{29}+49280M_1^{28}$$
$$+\ 175047M_1^{27}+88894M_1^{26}+209266M_1^{25}+119562M_1^{24}+31801M_1^{23}+71424M_1^{22}-352732M_1^{21}$$
$$-\ 180288M_1^{20}-267574M_1^{19}-229916M_1^{18}+162083M_1^{17}+74554M_1^{16}+72416M_1^{15}+55494M_1^{14}$$
$$+\ 64929M_1^{13}+48096M_1^{12}+52643M_1^{11}+62038M_1^{10}-129772M_1^9-106250M_1^8+45377M_1^7$$
$$\left.+\ 32564M_1^6-3374M_1^5-2092M_1^4+700M_1^3+740M_1^2-120M_1-120\right)$$
$$-\frac{\left(M_1^2-1\right)^2}{15M_1^8\left(M_1^2+1\right)^{11/2}\left(M_1^4+M_1^2-1\right)^5}\left(40M_1^{38}+440M_1^{36}+4147M_1^{34}+19113M_1^{32}+43928M_1^{30}\right.$$
$$+\ 56281M_1^{28}+23001M_1^{26}-83283M_1^{24}-134320M_1^{22}+19690M_1^{20}+98880M_1^{18}+5915M_1^{16}$$
$$\left.+\ 13318M_1^{14}-25313M_1^{12}-34293M_1^{10}+35249M_1^8-8726M_1^6+678M_1^4-215M_1^2+30\right)$$
$$-\frac{\left(M_1^2-1\right)^{10}\left(M_1^6-15M_1^2-2\right)}{2M_1^9\left(M_1^2+1\right)^7}\ln\left(\frac{M_1+1}{M_1-1}\right)+\frac{\left(M_1^2-1\right)}{2M_1^9\left(M_1^2+1\right)^7}\left(M_1^{24}+9M_1^{22}+117M_1^{20}\right.$$
$$+\ 441M_1^{18}+756M_1^{16}+1890M_1^{14}+378M_1^{12}+1386M_1^{10}-423M_1^8+117M_1^6-63M_1^4-3M_1^2+2\right)$$
$$\times\ln\left(\frac{M_1^2-1}{M_1^2+1}\right)+\frac{\left(M_1^2-1\right)}{M_1^9\left(M_1^2+1\right)^7}\left(M_1^{24}+9M_1^{22}+117M_1^{20}+441M_1^{18}+756M_1^{16}+1890M_1^{14}\right.$$
$$+\ 378M_1^{12}+1386M_1^{10}-423M_1^8+117M_1^6-63M_1^4-3M_1^2+2\left.\right)\ln\left(M_1+\sqrt{M_1^2+1}\right)$$
$$+\frac{2\left(M_1^2-1\right)}{M_1^3\left(M_1^2+1\right)^7}\left(9M_1^{16}+48M_1^{14}+196M_1^{12}+576M_1^{10}+414M_1^8+1008M_1^6-108M_1^4\right.$$
$$\left.+\ 288M_1^2-127\right)\ln\left(\frac{\sqrt{M_1^4+M_1^2-1}}{M_1\sqrt{M_1^2+1}+1}\right)+\frac{\left(M_1^2-1\right)}{4M_1^4\left(M_1^2+1\right)^7\left(M_1^4+M_1^2-1\right)^{9/2}}\left(12M_1^{36}+261M_1^{34}\right.$$
$$+\ 1683M_1^{32}+6954M_1^{30}+19015M_1^{28}+26608M_1^{26}+9061M_1^{24}-18794M_1^{22}-38689M_1^{20}$$

$$- 37546M_1^{18} + 27459M_1^{16} + 48054M_1^{14} - 20787M_1^{12} - 5008M_1^{10} + 5839M_1^8 - 14390M_1^6$$
$$+ 11585M_1^4 - 3067M_1^2 + 182\Big) \ln\left(\frac{\sqrt{M_1^4 - 1}}{\sqrt{M_1^4 + M_1^2 - 1} + M_1}\right). \tag{B15}$$

The total vorticity downstream is

$$W_{3D}(\gamma - 1 \ll 1, M_1)\frac{(M_1 - 1)^2}{60M_1^8\left(M_1^2 + 1\right)^6\left(M_1^4 + M_1^2 - 1\right)^4}\left(48M_1^{38} - 96M_1^{37} + 492M_1^{36} - 912M_1^{35}\right.$$
$$+ 3268M_1^{34} - 2065M_1^{33} + 9566M_1^{32} + 15942M_1^{31} + 20406M_1^{30} + 85161M_1^{29} + 49280M_1^{28}$$
$$+ 175047M_1^{27} + 88894M_1^{26} + 209266M_1^{25} + 119562M_1^{24} + 31801M_1^{23} + 71424M_1^{22} - 352732M_1^{21}$$
$$- 180288M_1^{20} - 267574M_1^{19} - 229916M_1^{18} + 162083M_1^{17} + 74554M_1^{16} + 72416M_1^{15} + 55494M_1^{14}$$
$$+ 64929M_1^{13} + 48096M_1^{12} + 52643M_1^{11} + 62038M_1^{10} - 129772M_1^9 - 106250M_1^8 + 45377M_1^7$$
$$+ 32564M_1^6 - 3374M_1^5 - 2092M_1^4 + 700M_1^3 + 740M_1^2 - 120M_1 - 120\Big)$$
$$- \frac{\left(M_1^2 - 1\right)^2}{15M_1^8\left(M_1^2 + 1\right)^{11/2}\left(M_1^4 + M_1^2 - 1\right)^4}\left(55M_1^{34} + 420M_1^{32} + 3900M_1^{30} + 16026M_1^{28} + 31661M_1^{26}\right.$$
$$+ 39070M_1^{24} + 15550M_1^{22} - 57440M_1^{20} - 62040M_1^{18} + 22720M_1^{16} + 15890M_1^{14} + 12680M_1^{12}$$
$$+ 15355M_1^{10} - 27196M_1^8 + 8244M_1^6 - 490M_1^4 + 185M_1^2 - 30\Big)$$
$$- \frac{\left(M_1^2 - 1\right)^{10}\left(M_1^6 - 15M_1^2 - 2\right)}{2M_1^9\left(M_1^2 + 1\right)^7}\ln\left(\frac{M_1 + 1}{M_1 - 1}\right) + \frac{\left(M_1^2 - 1\right)}{2M_1^9\left(M_1^2 + 1\right)^7}\left(M_1^{24} + 9M_1^{22} + 117M_1^{20}\right.$$
$$+ 441M_1^{18} + 756M_1^{16} + 1890M_1^{14} + 378M_1^{12} + 1386M_1^{10} - 423M_1^8 + 117M_1^6 - 63M_1^4 - 3M_1^2 + 2\Big)$$
$$\times \ln\left(\frac{M_1^2 - 1}{M_1^2 + 1}\right) + \frac{\left(M_1^2 - 1\right)}{M_1^9\left(M_1^2 + 1\right)^7}\left(M_1^{24} + 9M_1^{22} + 117M_1^{20} + 441M_1^{18} + 756M_1^{16} + 1890M_1^{14}\right.$$
$$+ 378M_1^{12} + 1386M_1^{10} - 423M_1^8 + 117M_1^6 - 63M_1^4 - 3M_1^2 + 2\Big)\ln\left(M_1 + \sqrt{M_1^2 + 1}\right)$$
$$+ \frac{8\left(M_1^2 - 1\right)}{M_1^3\left(M_1^2 + 1\right)^7}\left(3M_1^{16} + 12M_1^{14} + 50M_1^{12} + 144M_1^{10} + 100M_1^8 + 252M_1^6 - 26M_1^4 + 72M_1^2 - 31\right)$$
$$\times \ln\left(\frac{\sqrt{M_1^4 + M_1^2 - 1}}{M_1\sqrt{M_1^2 + 1} + 1}\right) + \frac{\left(M_1^2 - 1\right)}{4M_1^4\left(M_1^2 + 1\right)^7\left(M_1^4 + M_1^2 - 1\right)^{9/2}}\left(12M_1^{36} + 261M_1^{34} + 1683M_1^{32}\right.$$
$$+ 6954M_1^{30} + 19015M_1^{28} + 26608M_1^{26} + 9061M_1^{24} - 18794M_1^{22} - 38689M_1^{20} - 37546M_1^{18}$$
$$+ 27459M_1^{16} + 48054M_1^{14} - 20787M_1^{12} - 5008M_1^{10} + 5839M_1^8 - 14390M_1^6 + 11585M_1^4$$
$$- 3067M_1^2 + 182\Big)\ln\left(\frac{\sqrt{M_1^4 - 1}}{\sqrt{M_1^4 + M_1^2 - 1} + M_1}\right). \tag{B16}$$

4. Density amplification

The density perturbations generated by the shock front can be split into the entropic (long- and short-wavelength intervals) and acoustic perturbations. The strong shock limits for the long and short wavelengths are

$$G_{3D}^l(\gamma, M_1 \gg 1) \cong -\frac{\sqrt{2}(\gamma - 1)^{3/2}}{\sqrt{\gamma}} + (\gamma + 1)(2\gamma - 1)\left(\frac{\gamma - 1}{2\gamma}\right)^{3/2}\ln\left(\frac{\gamma + 1}{\gamma - 1}\right), \tag{B17}$$

$$G_{3D}^s(\gamma, M_1 \gg 1) \cong -\frac{(\gamma - 1)(3\gamma^3 - 5\gamma^2 - \gamma + 1)}{\gamma(2 - \gamma)} + \frac{(6\gamma^2 - 7\gamma - 7)(\gamma - 1)^{3/2}}{(2 - \gamma)\sqrt{2\gamma}}$$
$$- \frac{(\gamma + 1)(3\gamma - 2)(\gamma - 1)^{3/2}}{\sqrt{2\gamma}}\ln\left[\frac{\gamma(\gamma - 1) + \sqrt{2\gamma(\gamma - 1)}}{\gamma(\gamma + 1)}\right]. \tag{B18}$$

The acoustic contributions agree with Eq. (B3). The total density amplification is the sum of the contributions given above plus Eq. (B3):

$$G_{3\mathrm{D}}(\gamma, M_1 \gg 1) \cong -\frac{6\gamma^4 - 14\gamma^3 + 3\gamma^2 + 6\gamma - 2}{\gamma(2-\gamma)} + (\gamma+1)(2\gamma-1)\left(\frac{\gamma-1}{2\gamma}\right)^{3/2} \ln\left(\frac{\gamma+1}{\gamma-1}\right) + \frac{(12\gamma^3 - 20\gamma^2 - 13\gamma + 16)}{(2-\gamma)}\sqrt{\frac{\gamma-1}{2\gamma}} + \frac{\sqrt{2}(\gamma+1)(3\gamma-1)(\gamma-1)^{3/2}}{\sqrt{\gamma}} \ln\left[\frac{\gamma(\gamma-1)+\sqrt{2\gamma(\gamma-1)}}{\gamma(\gamma+1)}\right]. \tag{B19}$$

The highly compressible limit ($\gamma \to 1$) is given by the following expressions for the long- and short-wavelength intervals:

$$G^{l}_{3\mathrm{D}}(\gamma - 1 \ll 1, M_1) \cong \left\{ \frac{\left(M_1^2-1\right)^3\left(M_1^4+M_1^2-1\right)^3\left(M_1^8+6M_1^4+1\right)}{M_1^7\left(M_1^6+2M_1^4-1\right)^3} \ln\left(M_1+\sqrt{M_1^2+1}\right) - \frac{\left(M_1^2-1\right)^3\sqrt{M_1^2+1}\left(3M_1^{18}+2M_1^{16}+10M_1^{12}-12M_1^{10}-21M_1^8+24M_1^6+4M_1^4-15M_1^2+5\right)}{3M_1^6\left(M_1^6+2M_1^4-1\right)^3} + \frac{4\left(M_1^2-1\right)^3\left(M_1^4+1\right)\left(M_1^4+M_1^2-1\right)^3}{M_1^5\left(M_1^6+2M_1^4-1\right)^3} \ln\left(\frac{\sqrt{M_1^4+M_1^2-1}}{M_1\sqrt{M_1^2+1}+1}\right) \right\} (\gamma-1)^2, \tag{B20}$$

$$\begin{aligned} G^{s}_{3\mathrm{D}}(\gamma - 1 \ll 1, M_1) \cong \Bigg\{ & -\frac{M_1^2-1}{3M_1^{10}\left(M_1^2+1\right)^{7/2}\left(M_1^4+M_1^2-1\right)^3}\left(8M_1^{28}+61M_1^{26}+423M_1^{24}\right. \\ & + 1016M_1^{22}+381M_1^{20}-887M_1^{18}-1258M_1^{16}-1230M_1^{14}+1724M_1^{12}+1509M_1^{10}-1783M_1^8 \\ & \left. + 454M_1^6-65M_1^4+37M_1^2-6\right) + \frac{M_1-1}{3M_1^{10}\left(M_1^2+1\right)^4\left(M_1^4+M_1^2-1\right)^2}\left(4M_1^{27}-12M_1^{26}\right. \\ & + 37M_1^{25}-77M_1^{24}+167M_1^{23}-158M_1^{22}+251M_1^{21}+322M_1^{20}-94M_1^{19}+981M_1^{18} \\ & - 448M_1^{17}+412M_1^{16}-338M_1^{15}-124M_1^{14}-16M_1^{13}-1224M_1^{12}+416M_1^{11}-754M_1^{10} \\ & \left. + 123M_1^9+1515M_1^8-189M_1^7-446M_1^6+21M_1^5+38M_1^4+2M_1^3-31M_1^2+6\right) \\ & - \frac{\left(M_1^2-1\right)^8\left(M_1^6-11M_1^2-2\right)}{2M_1^{11}\left(M_1^2+1\right)^5}\ln\left(\frac{M_1+1}{M_1-1}\right) + \frac{1}{2M_1^{11}\left(M_1^2+1\right)^5}\left(M_1^{22}+8M_1^{20}+77M_1^{18}\right. \\ & \left. + 182M_1^{16}+70M_1^{14}+280M_1^{12}-434M_1^{10}+140M_1^8-103M_1^6+32M_1^4+5M_1^2-2\right) \\ & \times \ln\left(\frac{M_1^2+1}{M_1^2-1}\right) + \frac{1}{M_1^{11}\left(M_1^2+1\right)^5}\left(M_1^{22}+8M_1^{20}+77M_1^{18}+182M_1^{16}+70M_1^{14}\right. \\ & \left. + 280M_1^{12}-434M_1^{10}+140M_1^8-103M_1^6+32M_1^4+5M_1^2-2\right)\ln\left(\sqrt{M_1^2+1}+M_1\right) \\ & + \frac{4\left(4M_1^{14}+15M_1^{12}+38M_1^{10}+73M_1^8-56M_1^6+49M_1^4-82M_1^2+23\right)}{M_1^5\left(M_1^2+1\right)^5} \\ & \times \ln\left(\frac{\sqrt{M_1^4+M_1^2-1}}{M_1\sqrt{M_1^2+1}+1}\right) - \frac{1}{M_1^6\left(M_1^2+1\right)^5\left(M_1^4+M_1^2-1\right)^{5/2}}\left(-3M_1^{26}-47M_1^{24}-180M_1^{22}\right. \\ & - 439M_1^{20}-555M_1^{18}+408M_1^{16}+1048M_1^{14}-146M_1^{12}+39M_1^{10}-267M_1^8-724M_1^6+857M_1^4 \\ & \left. - 265M_1^2+18\right)\ln\left(\frac{\sqrt{M_1^4-1}}{\sqrt{M_1^4+M_1^2-1}+M_1}\right) \Bigg\} (\gamma-1)^2, \end{aligned} \tag{B21}$$

and the acoustic part is equivalent to that shown in Eq. (B7).

[1] E. E. Meshkov, Fluid Dyn. **4**, 101 (1969).
[2] S. Barre, D. Alem, and J. P. Bonnet, AIAA J. **34**, 968 (1996).
[3] G. Dimonte and R. Tipton, Phys. Fluids **18**, 85101 (2006).
[4] N. K.-R. Kevlahan and R. E. Pudritz, Astrophys. J. **702**, 39 (2009).
[5] H. S. Ribner, N. A. C. A. Report No. 3255 (1954).
[6] F. K. Moore, N. A. C. A. Report No. 2879 (1953).
[7] H. S. Ribner, AIAA J. **25**, 436 (1987).
[8] S. Lee, S. K. Lele, and P. Moin, J. Fluid Mech. **251**, 533 (1993).
[9] S. Lee, S. K. Lele, and P. Moin, J. Fluid Mech. **340**, 225 (1997).
[10] K. Mahesh, S. Lee, S. K. Lele, and P. Moin, J. Fluid Mech. **300**, 383 (1995).
[11] K. Mahesh, S. K. Lele, and P. Moin, J. Fluid Mech. **334**, 353 (1997).
[12] J. Larsson and S. K. Lele, Phys. Fluids **21**, 126101 (2009).
[13] D. Rotman, Phys. Fluids **3**, 1792 (1991).
[14] G. Hazak, A. L. Velikovich, J. H. Gardner, and J. P. Dahlburg, Phys. Plasmas **5**, 4357 (1998).
[15] A. L. Velikovich, J. G. Wouchuk, C. Huete Ruiz de Lira, N. Metzler, S. Zalesak, and A. J. Schmitt, Phys. Plasmas **14**, 072706 (2007).
[16] T. R. Boehly, V. N. Goncharov, W. Seka, M. A. Barrios, P. M. Celliers, D. G. Hicks, G. W. Collins, S. X. Hu, J. A. Marozas, and D. D. Meyerhofer, Phys. Rev. Lett. **106**, 195005 (2011).
[17] J. G. Wouchuk, C. Huete Ruiz de Lira, and A. L. Velikovich, Phys. Rev. E **79**, 066315 (2009).
[18] C. Huete Ruiz de Lira, Phys. Scr., T **142**, 014022 (2010).
[19] C. Huete Ruiz de Lira, A. L. Velikovich, and J. G. Wouchuk, Phys. Rev. E **83**, 056320 (2011).
[20] A. L. Velikovich, C. Huete, and J. G. Wouchuk, Phys. Rev. E **85**, 016301 (2012).
[21] J. G. Wouchuk, C. Huete, and A. L. Velikovich, Proceedings of the Shock Compression of Condensed Matter – 2011, edited by M. L. Elert, W. T. Buttler, J. P. Borg, J. L. Jordan, and T. J. Vogler, AIP Conf. Proc., New York, 2012 (to be published).
[22] P. M. Zaidel, J. Appl. Math. Mech. **24**, 316 (1960).
[23] M. G. Briscoe and A. A. Kovitz, J. Fluid Mech. **31**, 529 (1968).
[24] J. G. Wouchuk, Phys. Rev. E **63**, 056303 (2001).
[25] J. G. Wouchuk and J. Lopez Cavada, Phys. Rev. E **70**, 046303 (2004).
[26] Y. B. Zel'Dovich and Y. P. Raizer, *Physics of Shock Waves and High-temperature Hydrodynamic Phenomena* (Dover, New York, 2002).
[27] B. Davies, *Integral Transforms and their Applications* (Springer, New York, 2002).
[28] A. L. Velikovich, Phys. Fluids **8**, 1666 (1996).
[29] J. G. Wouchuk, Phys. Plasmas **8**, 2890 (2001).
[30] L. D. Landau and E. M. Lifshitz, *Fluid Mechanics* (Pergamon, New York, 1987).